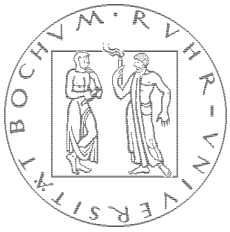

Ruhr University Bochum
Lehrstuhl für Technische Mechanik

Preprint 03-2005

A novel algorithmic framework for the numerical implementation of locally embedded strong discontinuities

J. Mosler

This is a preprint of an article published in:

Computer Methods in Applied Mechanics and Engineering, Vol. 194, Issues 45-47, 4731-4757 (2005)

A novel algorithmic framework for the numerical implementation of locally embedded strong discontinuities

J. Mosler

Lehrstuhl für Technische Mechanik
Ruhr University Bochum
Universitätsstr. 150,D-44780 Bochum, Germany
E-Mail: mosler@tm.bi.ruhr-uni-bochum.de
URL: www.tm.bi.ruhr-uni-bochum.de/mosler

SUMMARY

In this paper, a novel algorithmic framework for the numerical modeling of locally embedded strong discontinuities suitable for the analysis of material failure such as cracking in brittle structures or shear bands in soils is proposed. Based on the enhanced assumed strain (EAS) concept, the final failure kinematics of solids, approximated by discontinuous displacement fields, are incorporated into the finite element formulation. In contrast to previous works, the discontinuous part of the deformation mapping is condensed out at the material level without employing the standard static condensation technique. As a consequence, the resulting constitutive equations are formally identical to those of standard plasticity models. Hence, the return-mapping algorithm is applied to the numerical implementation. Only slight modifications of this, by now classical, algorithm are necessary. The proposed framework is applicable to any constitutive equation characterizing the inelastic part of deformation. Referring to the yield (failure) function and the evolution equations, no special assumption has to be made. Despite the differences between the presented numerical framework and the original implementation of the strong discontinuity approach (SDA), it is shown that both finite element models are completely equivalent. The applicability of the novel algorithmic formulation and its numerical performance are investigated by means of two two-dimensional as well as by means of a fully three-dimensional numerical analysis of shear band formation.

1 INTRODUCTION

Modeling of strain-localization phenomena such as cracking in brittle structures or the formation of shear bands in soils still represents a challenge to the scientific community. According to [1], an efficient approach suitable for the analysis of such phenomena should account for the multiscale character of the underlying physical problem (the width of the failure zone, e.g. the width of a shear band, is several dimensions smaller than the respective engineering structure) and should avoid the mesh dependence of the numerically computed results as reported in [2, 3]. Most approaches complying with the described restrictions are based on the incorporation of the small-scale kinematics, e.g. shear band sliding, into a large-scale macroscopic material model, see, e.g. References [4–10]. In these works, small-scale kinematics are captured by an enriched displacement field or a strain field, respectively.

In recent years, finite element formulations based on discontinuous displacement fields have become very popular for the analysis of strain-localization phenomena [7, 11–17]. These models, which pertain to the just mentioned multiscale approaches, are characterized by the approximation of the final failure kinematics of solids, e.g. crack opening in quasi brittle materials or shear band formation in metallic materials, by means of discontinuous displacement fields, embedded within the finite elements undergoing localization. The incorporation of strong discontinuities, i.e. discontinuous displacement fields, into standard finite elements based on continuous, resp. smooth, deformation mappings can be achieved by means of two different concepts.

On the one hand, it is possible to enrich the global displacement field using additional degrees of freedom. These degrees are associated with displacement jumps. An efficient framework to enhance a displacement field has been presented in [18, 19]. In these references, standard finite element interpolations are enriched only in the region of interest, e.g. the crack tip, by locally defined shape functions and additional degrees of freedom. This approach, also referred as to PUFEM (Partition of Unity Finite Element Method), has been applied to the modeling of strain-localization phenomena such as cracks in [7, 14, 20, 21].

On the other hand, the final failure kinematics of solids can be incorporated into a finite element formulation by adopting the Enhanced Assumed Strain (EAS) concept as proposed in [22, 23]. Following [4], only the enhanced strains induced by discontinuous deformation mappings appear explicitly in this approach. The global displacement field is unchanged. Consequently, and in contrast to numerical models based on the PUFEM, the respective field of the displacement jump is approximated in a local, i.e. in an incompatible fashion. Hence, the amplitude of the displacement discontinuity is discontinuous across the edge of two neighboring finite elements. According to the underlying EAS concept, most finite element formulations which are in line with [4] are based on the standard static condensation technique, see, e.g. References [6, 11–13, 16, 24, 25]. In these works, the discontinuity of the deformation mapping is condensed out at the element level. No additional degrees of freedom have to be introduced on the global finite element level. As a consequence, the computational costs resulting from the numerical implementation of these models are significantly less than those associated with the PUFEM.

A new algorithmic formulation for the numerical implementation of locally (incompatible) embedded strong discontinuities has been proposed in [26, 27]. A similar approach was recently presented in [15]. However, the formulation [15] is restricted to Constant Strain Triangle (CST) elements. In contrast to the strong discontinuity models [6, 11–13, 16, 24, 25], the numerical formulations suggested in [15, 26, 27] are not based on the static condensation technique. More precisely, the parameters defining the displacement jump within the finite element are condensed out at the material point level. These approaches result in linearized constitutive equations formally identical to those of standard (local) continuum models. Therefore, the by now well-known return mapping algorithm [28, 29] can be applied to solve the resulting nonlinear set of differential equations. Only minor modifications of material subroutines designed for standard plasticity models are required. Clearly, this represents an important advantage of the finite element formulations proposed in [15, 26, 27] in comparison to the original one presented in [4, 11, 12]. The applicability of this new algorithmic framework as well as its performance and numerical robustness have been demonstrated by means of fully three-dimensional analyses of pull-out tests of a steel anchor embedded within a concrete block [17, 30].

Despite the differences between the finite element formulation presented more recently [15, 26, 27] and the original implementation of the strong discontinuity approach (SDA) [4, 11, 12], in the case of constant strain elements, both finite element models are completely equivalent (see e.g. [15, 26, 31, 32]). However, as mentioned in [17, 31, 32], for non-constant strain interpolations, e.g. 4-node plane stress elements or 8-node brick elements, this identity does

not hold.

In this paper, a novel algorithmic framework for the numerical modeling of locally embedded strong discontinuities suitable for the analysis of material failure is proposed. Following [15, 26, 31, 32], the parameters defining the displacement jump within the finite element are condensed out at the material point level. Hence, as mentioned before, the resulting constitutive equations are formally identical to those of standard (local) continuum models, and standard solution procedures such as the return-mapping algorithm can be applied to the numerical implementation. However, in contrast to the previous works [15, 26, 31, 32], the presented finite element is equivalent to the original numerical formulation as proposed in [4, 11, 12], even in the case of non-constant strain interpolated elements such as the 4-node plane stress element or the 8-node brick element. As a consequence, the presented novel algorithmic formulation combines the advantages of the finite element models [15, 26, 31, 32] by leaving the original model itself (see [11, 12]) unaffected. Only the presented implementation differs from previous ones.

The paper is organized as follows: Section 2 is concerned with a brief summary of the basic kinematics associated with the strong discontinuity approach. The constitutive equations are contained in Section 3. Referring to the yield function and the evolution equations, no special assumption has to be made. In Section 4, the new algorithmic framework for the numerical implementation of locally embedded strong discontinuities is presented. At first, attention is restricted to constant strain elements. For these element types, the equivalence between the new implementation and the original one as proposed in [4, 11] is shown briefly (Subsection 4.1). Subsequently, the numerical model is extended to arbitrary finite elements (Subsection 4.2). Also, in this case the equivalence between both numerical implementations mentioned previously is illustrated. The applicability of the novel algorithmic formulation and its numerical performance are investigated by means of two two-dimensional (Subsection 5.1 and Subsection 5.3) as well as by means of a fully three-dimensional (Subsection 5.2) numerical analysis of shear band formation.

2 KINEMATICS INDUCED BY DISCONTINUOUS DEFORMATION MAPPINGS

In this section, a short summary of the kinematics associated with the Strong Discontinuity Approach (SDA) is given. For further details, refer to [6, 12, 31, 33].

A domain $\Omega \subset \mathbb{R}^3$ (more precisely, an open bounded set) is assumed to be separated into two parts Ω^- and Ω^+ by means of a $\mathcal{C}^\infty$ hyperplane $\partial_s\Omega$ (see Figure 1). From a physical point

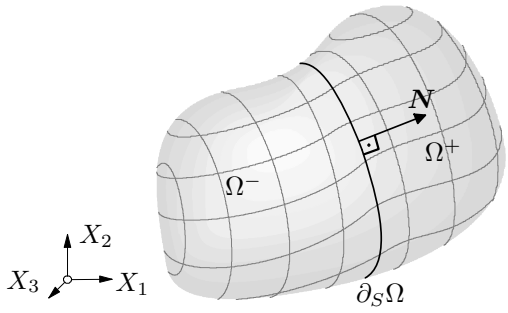

Figure 1: Body $\Omega \subset \mathbb{R}^3$ separated into two parts Ω^- and Ω^+ by a two-dimensional sub manifold $\partial_s\Omega$ of class $\mathcal{C}^\infty$.

of view, $\partial_{\mathrm{s}}\Omega$ represents a crack surface or a slip plane, respectively. Since $\partial_{\mathrm{s}}\Omega$ is a hyperplane of class $\mathcal{C}^\infty \subset \mathcal{C}^1$, the normal vector $\boldsymbol{N} \in N_{\boldsymbol{X}_0}$ of the submanifold $\partial_{\mathrm{s}}\Omega$ at the point $\boldsymbol{X}_0 \in \partial_{\mathrm{s}}\Omega$ is well-defined, i.e. $\dim N_{\boldsymbol{X}_0} = 1$. According to Figure 1, the introduction of a surface $\partial_{\mathrm{s}}\Omega$ implies a partition, i.e.

$$\Omega = \Omega^+ \dot\cup \Omega^- \dot\cup \partial_{\mathrm{s}}\Omega. \tag{1}$$

Following standard notation of set theory, $\dot\cup$ denotes the disjunct decomposition. Using $\partial_{\mathrm{s}}\Omega \subset \overline{\Omega^+}$ (the hyperplane is part of the closure of Ω^+), together with the fact that $\overline{\Omega^+}$ is connected, Ω^+ is defined by

$$\Omega^+ := \left\{ \boldsymbol{X} \in \Omega \mid \exists \boldsymbol{X}_0 = \boldsymbol{X}_0(\boldsymbol{X}) \in \partial_{\mathrm{s}}\Omega \text{ with } (\boldsymbol{X} - \boldsymbol{X}_0) \cdot \boldsymbol{N}|_{\boldsymbol{X}_0} > 0 \right\}. \tag{2}$$

In what follows, $\partial_{\mathrm{s}}\Omega$ is assumed to be planar. Hence, Definition (2) simplifies to (see [32])

$$\Omega^+ := \left\{ \boldsymbol{X} \in \Omega \mid (\boldsymbol{X} - \boldsymbol{X}_0) \cdot \boldsymbol{N}|_{\boldsymbol{X}_0} > 0 \right\}, \quad \boldsymbol{X}_0 \in \partial_{\mathrm{s}}\Omega. \tag{3}$$

In contrast to Definition (2), in the case of a planar surface $\partial_{\mathrm{s}}\Omega$, inequality $(\boldsymbol{X}-\boldsymbol{X}_0)\cdot\boldsymbol{N}|_{\boldsymbol{X}_0} > 0$ has to be checked only for an arbitrary point $\boldsymbol{X}_0$ belonging to $\partial_{\mathrm{s}}\Omega$. Hence, this format is well suitable for an efficient finite element formulation.

With Partition (1) and Definition (2), the left hand limit $\boldsymbol{u}^-(\boldsymbol{X}_0)$ and the right hand limit $\boldsymbol{u}^+(\boldsymbol{X}_0)$ of the displacement mapping $\boldsymbol{u} : \Omega \to \mathbb{R}^3$ at $\boldsymbol{X}_0 \in \partial_{\mathrm{s}}\Omega$ are obtained as

$$\boldsymbol{u}^\pm(\boldsymbol{X}_0) := \lim_{n\to\infty} \boldsymbol{u}(\boldsymbol{X}_n^\pm), \quad (\boldsymbol{X}_n^\pm)_{n\in\mathbb{N}} \in (\Omega^\pm)^{\mathbb{N}}, \quad \boldsymbol{X}_n^\pm \to \boldsymbol{X}_0 \ (n \to \infty). \tag{4}$$

Assuming the deformation to be discontinuous across $\partial_{\mathrm{s}}\Omega$, the discontinuity of $\boldsymbol{u}$ at $\boldsymbol{X}_0$ is defined as

$$[\![\boldsymbol{u}(\boldsymbol{X}_0)]\!] := \boldsymbol{u}^+(\boldsymbol{X}_0) - \boldsymbol{u}^-(\boldsymbol{X}_0) \quad \forall \boldsymbol{X}_0 \in \partial_{\mathrm{s}}\Omega. \tag{5}$$

Since in the following, attention is restricted to piecewise continuous displacement fields, the limits (4) exist, and, consequently, the discontinuity $[\![\boldsymbol{u}]\!]$ is well-defined.

In accordance with [4, 11, 12], a displacement field of the format

$$\boldsymbol{u} = \bar{\boldsymbol{u}} + [\![\boldsymbol{u}]\!] \ (H_{\mathrm{s}} - \varphi), \quad \text{with} \quad \bar{\boldsymbol{u}} \in \mathcal{C}^\infty(\Omega, \mathbb{R}^3), \ \varphi \in \mathcal{C}^\infty(\Omega, \mathbb{R}) \tag{6}$$

is adopted. In Equation (6), $H_{\mathrm{s}} : \Omega \to \{0; 1\}$ denotes the HEAVISIDE function with respect to the singular surface $\partial_{\mathrm{s}}\Omega$, i.e. the indicating function of the subset Ω^+, and φ represents a smooth ramp function necessary to prescribe the boundary conditions in terms of $\bar{\boldsymbol{u}}$ (see [12]). Clearly, the displacement field (6) is piecewise continuous. More precisely, $\boldsymbol{u}$ belongs to the space of bounded deformations as introduced in [34, 35]. Referring to the finite element method and following References [11, 31], φ is designed by the standard interpolation functions N_i associated with node i as

$$\varphi = \sum_{i=1}^{n_{\bar\Omega^+}} N_i. \tag{7}$$

Here and henceforth, the notation $\sum_{i=1}^{n_{\bar\Omega^+}}$ denotes the summation over all nodes of the respective finite element belonging to $\bar\Omega^+$.

Applying the generalized derivative D to the Heaviside function (see [36, 37]), which results in the identity $DH_{\mathrm{s}} = \boldsymbol{N}\ \delta_{\mathrm{s}}$, the deformation gradient is computed from Equation (6) as

$$\boldsymbol{F} = \boldsymbol{1} + \frac{\partial \bar{\boldsymbol{u}}}{\partial \boldsymbol{X}} + \frac{\partial\, [\![\boldsymbol{u}]\!]}{\partial \boldsymbol{X}} \ (H_{\mathrm{s}} - \varphi) + [\![\boldsymbol{u}]\!] \otimes \boldsymbol{N}\ \delta_{\mathrm{s}} - [\![\boldsymbol{u}]\!] \otimes \frac{\partial \varphi}{\partial \boldsymbol{X}}. \tag{8}$$

In Equation (8), δ_{s} represents the DIRAC-delta distribution with respect to $\partial_{\mathrm{s}}\Omega$. According to Equation (8), $\boldsymbol{F}$ consists of three parts: An absolutely continuous part $\boldsymbol{1} + \partial\bar{\boldsymbol{u}}/\partial\boldsymbol{X} - \partial\left[\!\left[\boldsymbol{u}\right]\!\right]/\partial\boldsymbol{X}\ \varphi - \left[\!\left[\boldsymbol{u}\right]\!\right] \otimes \partial\varphi/\partial\boldsymbol{X}$, a jump part $\partial\left[\!\left[\boldsymbol{u}\right]\!\right]/\partial\boldsymbol{X}\ H_{\mathrm{s}}$ and a singular distribution $\left[\!\left[\boldsymbol{u}\right]\!\right] \otimes \boldsymbol{N}\ \delta_{\mathrm{s}}$. This additive decomposition is always possible for the generalized derivative of mappings belonging to the space of bounded deformations.

As mentioned before, the incorporation of the discontinuous displacement field into the finite element formulation is achieved by adopting the EAS concept. Hence, the enriched displacement field is modeled in an incompatible sense. Consequently, it is admissible to neglect the gradient of the displacement discontinuity, i.e. $\partial\left[\!\left[\boldsymbol{u}\right]\!\right]/\partial\boldsymbol{X} = \boldsymbol{0}$, and to consider a deformation gradient of the type

$$\boldsymbol{F} = \boldsymbol{1} + \frac{\partial\bar{\boldsymbol{u}}}{\partial\boldsymbol{X}} + \left[\!\left[\boldsymbol{u}\right]\!\right] \otimes \boldsymbol{N}\ \delta_{\mathrm{s}} - \left[\!\left[\boldsymbol{u}\right]\!\right] \otimes \frac{\partial\varphi}{\partial\boldsymbol{X}}. \tag{9}$$

Clearly, only in the case $\partial\left[\!\left[\boldsymbol{u}\right]\!\right]/\partial\boldsymbol{X} = \boldsymbol{0}$ the gradient (9) results from the generalized derivative of a deformation mapping. However, $\boldsymbol{F}$ (according to Equation (9)) captures the highly localized deformations and complies with the restrictions of the EAS concept (see [22, 23]). From Equation (9), the linearized strain tensor is obtained as

$$\boldsymbol{\varepsilon} := \boldsymbol{\nabla}^{\mathrm{sym}}\boldsymbol{u} = \boldsymbol{\nabla}^{\mathrm{sym}}\bar{\boldsymbol{u}} - \underbrace{(\left[\!\left[\boldsymbol{u}\right]\!\right] \otimes \boldsymbol{\nabla}\varphi)^{\mathrm{sym}}}_{:=\,\tilde{\boldsymbol{\varepsilon}}} + (\left[\!\left[\boldsymbol{u}\right]\!\right] \otimes \boldsymbol{N})^{\mathrm{sym}}\ \delta_{\mathrm{s}}. \tag{10}$$

3 CONSTITUTIVE EQUATIONS

This section is concerned with the development of constitutive equations. Here and henceforth, inelastic deformations induced by plasticity or material damage are assumed to be restricted to $\partial_{\mathrm{s}}\Omega$, while the remaining part of the body $\Omega/\partial_{\mathrm{s}}\Omega$ unloads elastically [6, 11, 12, 31]. Hence, the stresses $\boldsymbol{\sigma}$ in $\Omega^{\pm}$ are computed from a free energy potential Ψ_{e} in standard manner, i.e. $\boldsymbol{\sigma} = \partial\Psi_{\mathrm{e}}/\partial\boldsymbol{\varepsilon}$. More precisely, HOOKE's law is adopted ($\boldsymbol{\sigma} = \mathbb{C} : \boldsymbol{\varepsilon}$).

Postulating the deformations in $\Omega^{\pm}$ to be purely (linear) elastic, irreversible processes are governed by the constitutive equations in $\partial_{\mathrm{s}}\Omega$. To develop these material laws, it is required to identify the thermodynamically conjugated variables. According to the extension of the principle of virtual work to domains exhibiting singular surfaces $\partial_{\mathrm{s}}\Omega$, the traction vector $\boldsymbol{t} := \boldsymbol{\sigma} \cdot \boldsymbol{N}$ acting in $\partial_{\mathrm{s}}\Omega$ is conjugated to the displacement jump $\left[\!\left[\boldsymbol{u}\right]\!\right]$ (see [11, 31]). Hence, a material law of the type

$$\boldsymbol{t}_{\mathrm{s}} = \boldsymbol{t}_{\mathrm{s}}(\left[\!\left[\boldsymbol{u}\right]\!\right]), \quad \text{with} \quad \boldsymbol{t}_{\mathrm{s}} := \boldsymbol{t}|_{\partial_{\mathrm{s}}\Omega} \tag{11}$$

represents an admissible choice (see [11, 30]). The coupling between the constitutive equations corresponding to $\Omega^{\pm}$ and those defined in $\partial_{\mathrm{s}}\Omega$ is provided by the condition of traction continuity across $\partial_{\mathrm{s}}\Omega$, i.e.

$$\boldsymbol{t}^{\pm}(\boldsymbol{X}_0) = \boldsymbol{t}(\boldsymbol{X}_0) \quad \forall \boldsymbol{X}_0 \in \partial_{\mathrm{s}}\Omega, \tag{12}$$

with $\boldsymbol{t}^{\pm}$ denoting the left hand and the right hand limits of the traction vector $\boldsymbol{t}$ according to Equation (4). Inserting Equation (11) into Equation (12) yields [31]

$$\boldsymbol{t}^{+} = \boldsymbol{t}_{\mathrm{s}}(\left[\!\left[\boldsymbol{u}\right]\!\right]) \quad \forall \boldsymbol{X}_0 \in \partial_{\mathrm{s}}\Omega. \tag{13}$$

As indicated in Equation (13), the displacement discontinuity $\left[\!\left[\boldsymbol{u}\right]\!\right]$ is governed by the stresses in $\Omega^{\pm}$. Using the positive definiteness of a norm $||\bullet||$, Equation (13) is rewritten as

$$\phi := ||\boldsymbol{t}^{+} - \boldsymbol{t}_{\mathrm{s}}|| = 0. \tag{14}$$

Note that Equation (14) is fully equivalent to the necessary condition of yielding known from standard plasticity models. Hence, it is possible to derive the constitutive model of the type (13) analogously to classical plasticity theory. For that purpose, a stored energy functional of the type

$$\Psi = \Psi_{\mathrm{reg}} + \Psi_{\mathrm{in}}\ \delta_{\mathrm{s}} \tag{15}$$

is adopted. According to Equation (15), and similarly to the strain field (10), an additive decomposition of the energy into a regularly distributed part Ψ_{reg} and a singular one Ψ_{in} is postulated. Assuming $[\![\boldsymbol{u}]\!]$ to be associated only with inelastic deformations, Ψ_{in} is specified by $\Psi_{\mathrm{in}} = \Psi_{\mathrm{in}}(\boldsymbol{\alpha}([\![\boldsymbol{u}]\!]))$ in terms of the displacement-like internal variable $\boldsymbol{\alpha} \in \mathbb{R}^n$ depending on the displacement discontinuity. Similarly to standard plasticity [28], the space of admissible stresses

$$\mathbb{E}_{\boldsymbol{t}} := \left\{(\boldsymbol{t}^+, \boldsymbol{q}) \in \mathbb{R}^3 \times \mathbb{R}^n \mid \phi(\boldsymbol{t}^+, \boldsymbol{q}) \leq 0\right\} \tag{16}$$

is defined by means of a yield (failure) function $\phi(\boldsymbol{t}^+, \boldsymbol{q})$, which depends on the traction vector $\boldsymbol{t}^+$ and a vector of stress-like hardening/softening parameters $\boldsymbol{q} = \boldsymbol{q}(\boldsymbol{\alpha})$ conjugated to $\boldsymbol{\alpha}$. For the special choice $\boldsymbol{\alpha} = [\![\boldsymbol{u}]\!]$ and $\phi(\boldsymbol{t}^+, \boldsymbol{q}) = ||\boldsymbol{t}^+ - \boldsymbol{q}||$, $\boldsymbol{q} = \boldsymbol{t}_{\mathrm{s}}$ and $\phi = 0$ is equivalent to the condition of traction continuity. Hence, the condition of traction continuity is included in the more general space of admissible stresses (16). Note that Definition (16) allows for the modeling of isotropic hardening/softening as well as the kinematical counterpart (see [31]).

Analogously to classical plasticity theory, the evolution equations associated with inelastic deformations, i.e. $[\![\boldsymbol{u}]\!]$, and the internal displacement-like variables $\boldsymbol{\alpha}$ are postulated as

$$[\![\dot{\boldsymbol{u}}]\!] = \lambda\ \partial_{\boldsymbol{t}^+} g \quad \text{and} \quad \dot{\boldsymbol{\alpha}} = \lambda\ \partial_{\boldsymbol{q}} h \quad \text{with} \quad \partial_{\boldsymbol{t}^+} g := \frac{\partial g}{\partial \boldsymbol{t}^+}. \tag{17}$$

Here and henceforth, the superposed dot is used to represent the time derivative. In Equations (17), $g = g(\boldsymbol{t}^+, \boldsymbol{q})$ and $h = h(\boldsymbol{t}^+, \boldsymbol{q})$ denote two potentials. Setting $g = \phi$ and $h = \phi$, associative evolution equations are obtained. Following standard plasticity theory, the plastic multiplier λ is computed from the consistency condition $\dot{\phi} = 0$.

So far, a general framework for the development of constitutive equations has been presented. In Section 4, the formation of shear bands in ductile materials is analyzed numerically. For that purpose, a VON MISES-type yield function ϕ is adopted. For fully three-dimensional stress states, the respective model is summarized in Appendix A. The two-dimensional plane stress counterpart is contained in Appendix B.

Remark 1. *So far only loading, i.e. $\lambda > 0$, has been considered. Since damage-induced strains and plastic deformations cannot be separated from each other for loading, the presented framework also holds for materials undergoing stiffness degradation. If damage accumulation is to be modeled, one part of the inelastic strains has to be connected to the elastic material properties, e.g. $\mathbb{C}$ (see [30, 31]).*

4 NUMERICAL IMPLEMENTATION

This section contains a novel algorithmic formulation for the modeling of locally embedded strong discontinuities. At first, the original finite element implementation as proposed in [11, 12] is summarized briefly. Starting from this specific SDA formulation, the new numerical framework is derived. After an explanation of the fundamentals, the respective finite element model is described in detail, at first for constant strain elements (Subsection 4.1). In Subsection 4.2, an extension for the most general case is given. No special assumption concerning

the polynomial order of the displacement field or the type of yield function and the evolution equations has to be made.

Since the additive decomposition of the strain tensor (10) is formally identical to the, by now standard, EAS concept (see [22, 23]), the original implementation of the strong discontinuity approach was based on this concept. Hence, the stationarity condition of the respective two field functional reads (see [11, 12])

$$\begin{aligned} \int_{\Omega^{\mathrm{e}}} \boldsymbol{\nabla}\bar{\boldsymbol{\eta}} : \boldsymbol{\sigma} \, \mathrm{d}V &= \int_{\Omega^{\mathrm{e}}} \boldsymbol{f} \cdot \bar{\boldsymbol{\eta}} \, \mathrm{d}V + \int_{\Gamma_\sigma} \boldsymbol{t}^* \cdot \bar{\boldsymbol{\eta}} \, \mathrm{d}\Gamma \\ \int_{\Omega^{\mathrm{e}}} \hat{\boldsymbol{\gamma}} : \boldsymbol{\sigma} \, \mathrm{d}V &= 0. \end{aligned} \tag{18}$$

In Equations (18), $\bar{\boldsymbol{\eta}}$ denotes a continuous test function, $\boldsymbol{f}$ body forces, $\boldsymbol{t}^*$ prescribed traction vectors acting on the NEUMANN boundary Γ_σ, Ω^{e} the domain of the respective finite element e and $\hat{\boldsymbol{\gamma}}$ represents the variations of the enhanced strains. As mentioned in Section 3, the stresses in Equations (18) are computed as

$$\boldsymbol{\sigma} = \mathbb{C} : [\boldsymbol{\nabla}^{\mathrm{sym}} \bar{\boldsymbol{u}} - (\llbracket \boldsymbol{u} \rrbracket \otimes \boldsymbol{\nabla}\varphi)^{\mathrm{sym}}] \quad \forall \boldsymbol{X} \in \Omega^{\pm}. \tag{19}$$

Following the EAS concept, the continuous, resp. smooth, displacement field $\bar{\boldsymbol{u}}$ is approximated by means of the standard shape functions N_i and nodal displacements $\bar{\boldsymbol{u}}_i^{\mathrm{e}}$, i.e.

$$\bar{\boldsymbol{u}} \approx \sum_{i=1}^{n_{\mathrm{node}}} N_i \, \bar{\boldsymbol{u}}_i^e \quad \Rightarrow \quad \boldsymbol{\nabla}\bar{\boldsymbol{u}} \approx \sum_{i=1}^{n_{\mathrm{node}}} \bar{\boldsymbol{u}}_i^e \otimes \boldsymbol{\nabla} N_i. \tag{20}$$

Adopting a GALERKIN-type interpolation of the continuous test functions, $\bar{\boldsymbol{\eta}}$ is assumed as

$$\bar{\boldsymbol{\eta}} = \sum_{i=1}^{n_{\mathrm{node}}} N_i \, \bar{\boldsymbol{\eta}}_i^e \quad \Rightarrow \quad \boldsymbol{\nabla}\bar{\boldsymbol{\eta}} = \sum_{i=1}^{n_{\mathrm{node}}} \bar{\boldsymbol{\eta}}_i^e \otimes \boldsymbol{\nabla} N_i. \tag{21}$$

In contrast to the standard EAS concept, a PETROV-GALERKIN discretization of the enhanced strains is applied. As proposed in [11], $\hat{\boldsymbol{\gamma}}$ is specified by (see also [13, 24])

$$\hat{\boldsymbol{\gamma}} = -\frac{A_{\mathrm{s}}}{V^{\mathrm{e}}} (\boldsymbol{N} \otimes \boldsymbol{\beta})^{\mathrm{sym}} + (\boldsymbol{N} \otimes \boldsymbol{\beta})^{\mathrm{sym}} \; \delta_{\mathrm{s}} \quad \boldsymbol{\beta} \in \mathbb{R}^3 \quad \text{(arbitrary)} \tag{22}$$

where V^{e} denotes the volume of the finite element, A_{s} the area of the localization surface $\partial_{\mathrm{s}}\Omega$ and $\boldsymbol{\beta}$ the variations of the displacement discontinuity. The main reason for choosing this specific tensor resulting in a nonsymmetric formulation is that a GALERKIN-type approximation does not pass the patch test (see [11]). Alternatively to Equation $(18)_2$ and (22), some authors, e.g. [12, 38], use the equivalent condition

$$\int_{\Omega^{\mathrm{e}}} \hat{\hat{\boldsymbol{\gamma}}} \cdot \boldsymbol{\sigma} \, \mathrm{d}V = \boldsymbol{0}, \tag{23}$$

with

$$\hat{\hat{\boldsymbol{\gamma}}} = -\frac{A_{\mathrm{s}}}{V} \boldsymbol{N} + \boldsymbol{N} \, \delta_{\mathrm{s}}. \tag{24}$$

Inserting Equation (22) into $(18)_2$ (or Equation (24) into (23)) leads to

$$\frac{1}{V^{\mathrm{e}}} \int_{\Omega^{\mathrm{e}}} \boldsymbol{t} \, \mathrm{d}V = \frac{1}{A_{\mathrm{s}}} \int_{\partial_{\mathrm{s}}\Omega} \boldsymbol{t}_{\mathrm{s}} \, \mathrm{d}A. \tag{25}$$

For further details, refer to [11, 12]. Hence, the L_2 orthogonality condition $(18)_2$ is equivalent to the weak form of traction continuity between $\Omega^{\pm}$ and $\partial_{\mathrm{s}}\Omega$. As a consequence, Equations (18) represent the standard weak form of equilibrium together with the condition of traction continuity.

So far, the original implementation of the strong discontinuity approach has only been summarized in a brief format. Next, the novel algorithmic framework is presented. At first the useful notation

$$\overline{(\bullet)} := \frac{1}{V^{\mathrm{e}}} \int_{\Omega^{\mathrm{e}}} (\bullet) \, \mathrm{d}V \tag{26}$$

is introduced, i.e. $\overline{(\bullet)}$ denotes the average value of the variable $(\bullet)$. According to Section 2, the displacement discontinuity is assumed to be constant ($\partial \left[\!\left[\boldsymbol{u}\right]\!\right] / \partial \boldsymbol{X} = \boldsymbol{0}$). This is characteristic for the SDA, see e.g. [6, 11–13, 15, 16, 24, 25]. Since $\boldsymbol{t}_{\mathrm{s}} = \boldsymbol{t}_{\mathrm{s}}(\boldsymbol{\alpha}(\left[\!\left[\boldsymbol{u}\right]\!\right]))$, the traction vector acting in $\partial_{\mathrm{s}}\Omega$ is constant as well. Hence, inserting Definition (26) into Equation (25) yields

$$\phi := ||\overline{\boldsymbol{t}} - \boldsymbol{t}_{\mathrm{s}}|| = 0. \tag{27}$$

Analogously to the strong form of traction continuity described in Section 3, the corresponding weak form is formally identical to the necessary condition of yielding known from standard plasticity theory. In contrast to Section 3, $\boldsymbol{t}^+$ is replaced by the average value $\overline{\boldsymbol{t}}$. Following the ideas presented in Section 3, the space of admissible stresses

$$\mathbb{E}_{\boldsymbol{t}} := \left\{ (\overline{\boldsymbol{t}}, \boldsymbol{q}) \in \mathbb{R}^3 \times \mathbb{R}^n \mid \phi(\overline{\boldsymbol{t}}, \boldsymbol{q}) \leq 0 \right\} \tag{28}$$

is introduced. Note that the internal stress-like variable $\boldsymbol{q}$ conjugated to $\boldsymbol{\alpha}$ depends on $\left[\!\left[\boldsymbol{u}\right]\!\right]$ via $\boldsymbol{q} = \boldsymbol{q}(\boldsymbol{\alpha}(\left[\!\left[\boldsymbol{u}\right]\!\right]))$. Consequently, $\boldsymbol{q}$ is constant with respect to $\boldsymbol{X}$. Clearly, the restriction $\phi(\bar{\boldsymbol{t}}, \boldsymbol{q}) \leq 0$ is more general than the weak form of traction continuity (27) and includes Equation (25) as a special case (see Section 3).

Next, the evolution equations have to be re-formulated. By comparing Equation (28) with Equation (16), two potentials g and h of the type $g = g(\overline{\boldsymbol{t}}, \boldsymbol{q})$ and $h = h(\overline{\boldsymbol{t}}, \boldsymbol{q})$ are introduced (see also Equations (17)). Applying the strong form of traction continuity to the evolution Equations (17), i.e. $\boldsymbol{t}^+ = \boldsymbol{t}_{\mathrm{s}}$, together with the corresponding weak form leading to $\boldsymbol{t}_{\mathrm{s}} = \overline{\boldsymbol{t}}$, the evolution equations

$$\left[\!\left[\dot{\boldsymbol{u}}\right]\!\right] = \lambda \, \partial_{\overline{\boldsymbol{t}}} g \quad \text{and} \quad \dot{\boldsymbol{\alpha}} = \lambda \, \partial_{\boldsymbol{q}} h \tag{29}$$

are obtained. In the case of associative evolution equations, g and h are set to ϕ. The whole set of equations describing the material response is summarized in Table 1.

4.1 Constant strain elements

Restricting attention to constant strain elements for now, i.e. $\boldsymbol{\nabla} \bar{\boldsymbol{u}} = \text{const}$, the stresses in $\Omega^{\pm}$ and the resulting tractions are constant as well (see Remark 2). Hence, the weak form of traction equilibrium (25) is equivalent to its corresponding strong form. As a consequence, the set of Equations (18) can be rewritten as

$$\begin{array}{lcl} \displaystyle\int_{\Omega^{\mathrm{e}}} \boldsymbol{\nabla} \bar{\boldsymbol{\eta}} : \boldsymbol{\sigma} \, \mathrm{d}V & = & \displaystyle\int_{\Omega^{\mathrm{e}}} \boldsymbol{f} \cdot \bar{\boldsymbol{\eta}} \, \mathrm{d}V + \int_{\Gamma_\sigma} \boldsymbol{t}^* \cdot \bar{\boldsymbol{\eta}} \, \mathrm{d}\Gamma \\ \phi(\boldsymbol{t}, \boldsymbol{q}) & = & 0. \end{array} \tag{35}$$

Following standard plasticity theory, the plastic multiplier λ is computed from the consistency condition as

$$\dot{\phi} = 0 \quad \Rightarrow \quad \lambda = \frac{\partial_{\boldsymbol{t}} \phi \cdot \left[\boldsymbol{N} \cdot \mathbb{C} : \boldsymbol{\nabla}^{\mathrm{sym}} \dot{\bar{\boldsymbol{u}}} \right]}{\partial_{\boldsymbol{t}} \phi \cdot \left[\boldsymbol{N} \cdot \mathbb{C} : (\partial_{\boldsymbol{t}} g \otimes \boldsymbol{\nabla} \varphi) \right] + \partial_{\boldsymbol{q}} \phi \cdot \boldsymbol{H} \cdot \partial_{\boldsymbol{q}} h}, \tag{36}$$

Table 1: Re-formulated constitutive equations for a strong discontinuity approach based finite element formulation.

1. Average value of the traction vector in $\Omega^{\pm}$

$$\overline{\boldsymbol{t}} = \frac{1}{V^{\mathrm{e}}} \int_{\Omega^{\mathrm{e}}} \boldsymbol{t} \, \mathrm{d}V \tag{30}$$

2. Space of admissible stresses

$$\mathbb{E}_{\boldsymbol{t}} := \left\{ (\overline{\boldsymbol{t}}, \boldsymbol{q}) \in \mathbb{R}^3 \times \mathbb{R}^n \mid \phi(\overline{\boldsymbol{t}}, \boldsymbol{q}) \leq 0 \right\} \tag{31}$$

for instance

$$\phi = ||\overline{\boldsymbol{t}}|| - q(\alpha([\![\boldsymbol{u}]\!])) \tag{32}$$

3. Evolution equation of the displacement discontinuity

$$[\![\dot{\boldsymbol{u}}]\!] = \lambda \, \partial_{\overline{\boldsymbol{t}}} g(\overline{\boldsymbol{t}}, \boldsymbol{q}) \tag{33}$$

for instance associativity, i.e. $g = \phi$

4. Evolution equation of the displacement-like internal variable $\boldsymbol{\alpha}$

$$\dot{\boldsymbol{\alpha}} = \lambda \, \partial_{\boldsymbol{q}} h(\overline{\boldsymbol{t}}, \boldsymbol{q}) \tag{34}$$

for instance associativity, i.e. $h = \phi$

with $\boldsymbol{H} := -\partial \boldsymbol{q}/\partial \boldsymbol{\alpha}$. From the stress rates

$$\dot{\boldsymbol{\sigma}} = \mathbb{C} : \left[\boldsymbol{\nabla}^{\mathrm{sym}} \dot{\bar{\boldsymbol{u}}} - \lambda \ (\partial_{\boldsymbol{t}} g \otimes \boldsymbol{\nabla}\varphi)^{\mathrm{sym}} \right], \tag{37}$$

together with Equation (36), the 4th-order tangent operator $\mathbb{C}_{\mathrm{T}}$ is obtained as

$$\mathbb{C}_{\mathrm{T}} := \frac{\mathrm{d}\boldsymbol{\sigma}}{\mathrm{d}\boldsymbol{\nabla}^{\mathrm{sym}} \bar{\boldsymbol{u}}} = \mathbb{C} - \frac{\mathbb{C} : (\partial_{\boldsymbol{t}} g \otimes \boldsymbol{\nabla}\varphi)^{\mathrm{sym}} \otimes (\partial_{\boldsymbol{t}} \phi \otimes \boldsymbol{N})^{\mathrm{sym}} : \mathbb{C}}{\partial_{\boldsymbol{t}} \phi \cdot [\boldsymbol{N} \cdot \mathbb{C} : (\partial_{\boldsymbol{t}} g \otimes \boldsymbol{\nabla}\varphi)] + \partial_{\boldsymbol{q}} \phi \cdot \boldsymbol{H} \cdot \partial_{\boldsymbol{q}} h}. \tag{38}$$

Inserting Equation (38) and (20) into the rate form of Equation $(35)_1$ leads to

$$\int_{\Omega^{\mathrm{e}}} \boldsymbol{\nabla}\bar{\boldsymbol{\eta}} : \mathbb{C}_{\mathrm{T}} : \boldsymbol{\nabla}^{\mathrm{sym}} \dot{\bar{\boldsymbol{u}}} \, \mathrm{d}V = \int_{\Omega^{\mathrm{e}}} \dot{\boldsymbol{f}} \cdot \bar{\boldsymbol{\eta}} \, \mathrm{d}V + \int_{\Gamma_\sigma} \dot{\boldsymbol{t}}^* \cdot \bar{\boldsymbol{\eta}} \, \mathrm{d}\Gamma. \tag{39}$$

Clearly, Equations (38) and (39) are formally identical to standard plasticity theory. Note that the stiffness matrix associated with Equation (39) is nonsymmetric, since for $\mathbb{C}_{\mathrm{T}}$ the identity $\{\mathbb{C}_{\mathrm{T}}\}_{ijkl} \neq \{\mathbb{C}_{\mathrm{T}}\}_{klij}$ does not hold. Even in the case of associative evolution equations, $\mathbb{C}_{\mathrm{T}}$ does not, in general, show this symmetry property. Only if the vectors $\boldsymbol{N}$ and $\boldsymbol{\nabla}\varphi$ are additionally linearly dependent, $\{\mathbb{C}_{\mathrm{T}}\}_{ijkl} = \{\mathbb{C}_{\mathrm{T}}\}_{klij}$, and a symmetric stiffness matrix is obtained. This results directly from the PETROV-GALERKIN discretization of the enhanced strains.

Remark 2. *According to Equation (20), $\boldsymbol{\nabla}\bar{\boldsymbol{u}} = const \ \Leftrightarrow \ \boldsymbol{\nabla} N_i = const.$ Since a ramp function of the format (7) has been adopted, $\boldsymbol{\nabla}\varphi = const.$ Using Equation (10), it follows that $\boldsymbol{\varepsilon} = const$ in $\boldsymbol{X}$ (note that $\boldsymbol{\nabla} [\![\boldsymbol{u}]\!] = \boldsymbol{0}$).*

4.2 Arbitrary finite elements

In Subsection 4.1, the fundamentals of the new algorithmic formulation suitable for the modeling of strong discontinuities in solids have been explained. In this subsection, the proposed concept is generalized for arbitrary finite elements. Additionally, the numerical implementation is presented in detail.

The starting point of the finite element model is the set of Equations (18). As mentioned before, alternatively to Equation $(18)_2$, the more general case

$$\begin{array}{lcl} \displaystyle\int_{\Omega^{\mathrm{e}}} \boldsymbol{\nabla}\bar{\boldsymbol{\eta}} : \boldsymbol{\sigma} \, \mathrm{d}V & = & \displaystyle\int_{\Omega^{\mathrm{e}}} \boldsymbol{f} \cdot \bar{\boldsymbol{\eta}} \, \mathrm{d}V + \int_{\Gamma_\sigma} \boldsymbol{t}^* \cdot \bar{\boldsymbol{\eta}} \, \mathrm{d}\Gamma \\ \phi(\bar{\boldsymbol{t}}, \boldsymbol{q}) & = & 0 \end{array} \tag{40}$$

is considered. According to computational plasticity, Problem (40) is approached by first solving Equation $(40)_2$ and subsequently Equation $(40)_1$ (compare to Subsection 4.1). First, the solution of Equation $(40)_2$ is computed. For that purpose a return-mapping algorithm is applied.

Assuming the inelastic deformations to be restricted to $\partial_{\mathrm{s}}\Omega$, together with the strain tensor (10), the updated stresses $\boldsymbol{\sigma}$ and the stress-like internal variables $\boldsymbol{q}$ at the end of the time interval $[t_n, t_{n+1}]$ are obtained as

$$\begin{array}{rcl} \boldsymbol{\sigma}(t_{n+1}) =: \boldsymbol{\sigma}_{n+1} & = & \mathbb{C} : (\boldsymbol{\nabla}^{\mathrm{sym}} \bar{\boldsymbol{u}}_{n+1} - \tilde{\boldsymbol{\varepsilon}}_{n+1}) \\ \boldsymbol{q}_{n+1} & = & \boldsymbol{q}(\boldsymbol{\alpha}_{n+1}). \end{array} \tag{41}$$

With the definition of a trial state

$$\begin{array}{rcl} \boldsymbol{\sigma}^{\mathrm{tr}}_{n+1} & := & \mathbb{C} : (\boldsymbol{\nabla}^{\mathrm{sym}} \bar{\boldsymbol{u}}_{n+1} - \tilde{\boldsymbol{\varepsilon}}_n) \\ \boldsymbol{q}^{\mathrm{tr}} & := & \boldsymbol{q}(\boldsymbol{\alpha}_n) \end{array} \tag{42}$$

characterized by pure elastic deformations ($\lambda = 0$, $[\![\dot{\boldsymbol{u}}]\!] = \boldsymbol{0}$), the discrete counterpart of the loading condition is given as

$$\phi(\overline{\boldsymbol{t}^{\mathrm{tr}}_{n+1}}, \boldsymbol{q}^{\mathrm{tr}}_{n+1}) =: \phi^{\mathrm{tr}} > 0, \quad \text{with} \quad \overline{\boldsymbol{t}^{\mathrm{tr}}_{n+1}} = \overline{\boldsymbol{N} \cdot \boldsymbol{\sigma}^{\mathrm{tr}}_{n+1}} = \boldsymbol{N} \cdot \overline{\boldsymbol{\sigma}^{\mathrm{tr}}_{n+1}}. \tag{43}$$

If inelastic loading is signaled by $\phi^{\mathrm{tr}}_{n+1} > 0$, the return-mapping algorithm will be performed (see [28]). For that purpose, a backward EULER integration is applied to the evolution of the displacement jump $[\![\boldsymbol{u}]\!]$ and to the evolution of the displacement-like internal variable $\boldsymbol{\alpha}$ (see Equations (29)) leading to

$$\Delta\,[\![\boldsymbol{u}]\!]_{n+1} = \Delta\lambda_{n+1}\ \partial_{\overline{\boldsymbol{t}}} g\Big|_{n+1} \quad \text{and} \quad \Delta\boldsymbol{\alpha}_{n+1} = \Delta\lambda_{n+1}\ \partial_{\boldsymbol{q}} h\big|_{n+1}\,. \tag{44}$$

Here and henceforth, the notations $\Delta(\bullet)_{n+1} := (\bullet)_{n+1} - (\bullet)_n$ and $\Delta\lambda_{n+1} = \lambda_{n+1}\ \Delta t_{n+1}$ are used. With Equation $(44)_1$, the increment of the regularly distributed enhanced strains (see Equation (10)) is obtained as

$$\Delta\tilde{\boldsymbol{\varepsilon}}_{n+1} = \Delta\lambda_{n+1}\ \left(\partial_{\overline{\boldsymbol{t}}} g\Big|_{n+1} \otimes \boldsymbol{\nabla}\varphi\right)^{\mathrm{sym}}. \tag{45}$$

Combining Equation (45) with Equation (41), the average value of the traction vector $\boldsymbol{t}$ at time t_{n+1} is computed as

$$\overline{\boldsymbol{t}_{n+1}} = \overline{\boldsymbol{N} \cdot \boldsymbol{\sigma}_{n+1}} = \boldsymbol{N} \cdot \overline{\boldsymbol{\sigma}^{\mathrm{tr}}_{n+1}} - \boldsymbol{N} \cdot \mathbb{C} : \overline{\Delta\tilde{\boldsymbol{\varepsilon}}_{n+1}} = \overline{\boldsymbol{t}^{\mathrm{tr}}_{n+1}} - \boldsymbol{N} \cdot \mathbb{C} : \overline{\Delta\tilde{\boldsymbol{\varepsilon}}_{n+1}}, \tag{46}$$

with

$$\overline{\Delta\tilde{\boldsymbol{\varepsilon}}_{n+1}} = \Delta\lambda_{n+1}\ \left(\partial_{\overline{\boldsymbol{t}}} g\Big|_{n+1} \otimes \overline{\boldsymbol{\nabla}\varphi}\right)^{\mathrm{sym}}. \tag{47}$$

Since Equations (46) and (47) are formally identical to their counterparts appearing in the standard return-mapping algorithm (see [28, 29]), the same solution strategy can be applied. For that purpose, the residuals

$$\begin{aligned} \boldsymbol{R}^{\boldsymbol{\varepsilon}} &:= -\overline{\tilde{\boldsymbol{\varepsilon}}_{n+1}} + \overline{\tilde{\boldsymbol{\varepsilon}}_n} + \overline{\Delta\tilde{\boldsymbol{\varepsilon}}_{n+1}}, \\ \boldsymbol{R}^{\boldsymbol{\alpha}} &:= -\boldsymbol{\alpha}_{n+1} + \boldsymbol{\alpha}_n + \Delta\boldsymbol{\alpha}_{n+1} \end{aligned} \tag{48}$$

are defined. Consequently, if inelastic loading is signalled, the nonlinear set of equations

$$\boldsymbol{R}^T := [\boldsymbol{R}^{\boldsymbol{\varepsilon}}; \boldsymbol{R}^{\boldsymbol{\alpha}}] = \boldsymbol{0} \quad \wedge \quad \phi_{n+1} = 0 \tag{49}$$

is solved iteratively. Note that

$$\begin{aligned} \mathrm{d}\overline{\boldsymbol{\sigma}_{n+1}} &= -\,\mathbb{C} : \mathrm{d}\overline{\tilde{\boldsymbol{\varepsilon}}_{n+1}} \quad \text{and} \quad \mathrm{d}\overline{\boldsymbol{t}_{n+1}} = -\boldsymbol{N} \cdot \mathbb{C} : \mathrm{d}\overline{\tilde{\boldsymbol{\varepsilon}}_{n+1}} \\ \mathrm{d}\boldsymbol{q}_{n+1} &= -\,\boldsymbol{H}_{n+1} \cdot \mathrm{d}\boldsymbol{\alpha}_{n+1} \end{aligned} \tag{50}$$

within a particular step of the return-mapping algorithm (see [28]) and consequently, $\overline{\boldsymbol{\sigma}_{n+1}}$, $\boldsymbol{q}_{n+1}$ and λ (or alternatively $\overline{\tilde{\boldsymbol{\varepsilon}}_{n+1}}$, $\boldsymbol{\alpha}_{n+1}$ and λ) represent the only independent unknown variables. Following the return-mapping algorithm, the solution of the problem defined by Equations (49) is computed by means of NEWTON's method. Hence, the linearizations of Equations (49) are required. Using Equations $(48)_1$, $(50)_1$ and (47), the linearization of $\boldsymbol{R}^{\boldsymbol{\varepsilon}}$ is computed as

$$\begin{aligned} \mathrm{d}\boldsymbol{R}^{\boldsymbol{\varepsilon}} = \quad & \left[\mathbb{C}^{-1} + \Delta\lambda_{n+1}\ \left(\partial^2_{\overline{\boldsymbol{t}}\otimes\overline{\boldsymbol{\sigma}}} g\Big|_{n+1} \otimes \overline{\boldsymbol{\nabla}\varphi}\right)^{\mathrm{sym}}\right] : \mathrm{d}\overline{\boldsymbol{\sigma}_{n+1}} \\ + \quad & \Delta\lambda_{n+1}\ \left(\partial^2_{\overline{\boldsymbol{t}}\otimes\boldsymbol{q}} g\Big|_{n+1} \otimes \overline{\boldsymbol{\nabla}\varphi}\right)^{\mathrm{sym}} \cdot \mathrm{d}\boldsymbol{q}_{n+1} \\ + \quad & \mathrm{d}\Delta\lambda_{n+1}\ \left(\partial_{\overline{\boldsymbol{t}}} g\Big|_{n+1} \otimes \overline{\boldsymbol{\nabla}\varphi}\right)^{\mathrm{sym}}. \end{aligned} \tag{51}$$

Analogously, $\mathrm{d}\boldsymbol{R}^{\boldsymbol{\alpha}}$ is obtained as

$$\begin{aligned}\mathrm{d}\boldsymbol{R}^{\boldsymbol{\alpha}} = & \quad \Delta\lambda_{n+1}\ \partial^2_{\boldsymbol{q}\otimes\overline{\boldsymbol{\sigma}}} h\Big|_{n+1} : \mathrm{d}\overline{\boldsymbol{\sigma}_{n+1}} \\ & + \left[\boldsymbol{H}^{-1}\big|_{n+1} + \Delta\lambda_{n+1}\ \partial^2_{\boldsymbol{q}\otimes\boldsymbol{q}} h\Big|_{n+1}\right]\cdot \mathrm{d}\boldsymbol{q}_{n+1} \\ & + \mathrm{d}\Delta\lambda_{n+1}\ \partial_{\boldsymbol{q}} h\big|_{n+1}\,.\end{aligned} \tag{52}$$

Note that the simple (double) contraction in Equation (51) is not the standard one. For instance, in CARTESIAN coordinates these operations result in

$$\begin{aligned}\left\{\left(\partial^2_{\overline{\boldsymbol{t}}\otimes\overline{\boldsymbol{\sigma}}} g\otimes\overline{\boldsymbol{\nabla}\varphi}\right)^{\mathrm{sym}} : \mathrm{d}\overline{\boldsymbol{\sigma}}\right\}_{il} &= \left(\partial^2_{\overline{t_i}\otimes\overline{\sigma_{jk}}} g\ \overline{\nabla\varphi}_l\right)^{\mathrm{sym}}\ \mathrm{d}\overline{\sigma_{jk}} \\ \left\{\left(\partial^2_{\overline{\boldsymbol{t}}\otimes\boldsymbol{q}} g\otimes\overline{\boldsymbol{\nabla}\varphi}\right)^{\mathrm{sym}}\cdot \mathrm{d}\boldsymbol{q}\right\}_{ik} &= \left(\partial^2_{\overline{t_i}\otimes q_j} g\ \overline{\nabla\varphi}_k\right)^{\mathrm{sym}}\ \mathrm{d}q_j.\end{aligned} \tag{53}$$

With the definitions

$$\boldsymbol{A}^{-1} := \left[\begin{array}{cc} \mathbb{C}^{-1} + \Delta\lambda\ \left(\partial^2_{\overline{\boldsymbol{t}}\otimes\overline{\boldsymbol{\sigma}}} g\otimes\overline{\boldsymbol{\nabla}\varphi}\right)^{\mathrm{sym}} & \Delta\lambda\ \left(\partial^2_{\overline{\boldsymbol{t}}\otimes\boldsymbol{q}} g\otimes\overline{\boldsymbol{\nabla}\varphi}\right)^{\mathrm{sym}} \\ \Delta\lambda\ \partial^2_{\boldsymbol{q}\otimes\overline{\boldsymbol{\sigma}}} h & \boldsymbol{H}^{-1} + \Delta\lambda\ \partial^2_{\boldsymbol{q}\otimes\boldsymbol{q}} h \end{array}\right]\Bigg|_{n+1}, \tag{54}$$

$$\boldsymbol{\nabla} M^T := \left[\left(\partial_{\overline{\boldsymbol{t}}} g\otimes\overline{\boldsymbol{\nabla}\varphi}\right)^{\mathrm{sym}};\quad \partial_{\boldsymbol{q}} h\right]\Big|_{n+1}, \tag{55}$$

$$\boldsymbol{\nabla}\phi^T := \left[\partial_{\overline{\boldsymbol{\sigma}}}\phi;\quad \partial_{\boldsymbol{q}}\phi\right]\big|_{n+1} \quad \text{and} \quad \boldsymbol{\Delta}^T := \left[\mathrm{d}\overline{\boldsymbol{\sigma}};\quad \mathrm{d}\boldsymbol{q}\right]|_{n+1}, \tag{56}$$

i.e. $\mathrm{d}\phi = \boldsymbol{\nabla}\phi^T\boldsymbol{\Delta}$, the increment of the plastic multiplier during an iteration cycle is computed as

$$\mathrm{d}\Delta\lambda_{n+1} = \frac{\phi_{n+1} - \boldsymbol{\nabla}\phi^T\ \boldsymbol{A}\ \boldsymbol{R}}{\boldsymbol{\nabla}\phi^T\ \boldsymbol{A}\ \boldsymbol{\nabla} M}. \tag{57}$$

Clearly, Equation (57) is formally identical to the standard return-mapping (see, e.g. [28, 29]). Hence, the implementation of the presented algorithm only requires minor modifications of material subroutines designed for (local) continuum plasticity models. Despite the similar form of the proposed numerical framework and the finite element formulation suggested in [30, 32], only for constant strain elements, i.e. $\overline{(\bullet)} = (\bullet)$, both models are equivalent.

Remark 3. *Many authors assume that the direction of the displacement jump is restricted by some constraints associated with the considered material. Frequently, the condition $\partial_{\overline{\boldsymbol{t}}} g/||\partial_{\overline{\boldsymbol{t}}} g||_2 \cdot \boldsymbol{N} = \text{const}$ is adopted (see, e.g. [13, 39, 40]). In a two-dimensional setting, this assumption results in $\partial_{\overline{\boldsymbol{t}}} g/||\partial_{\overline{\boldsymbol{t}}} g||_2 = \text{const}$. Hence, the amplitude of the displacement discontinuity represents the only unknown variable in the set of Equations (49) and, consequently, the nonlinear Problem (49) degenerates to a single scalar valued equation. Clearly, this represents the easiest case possible. However, for many materials, this restriction is unjustified or even wrong. Therefore, in the proposed algorithmic formulation, no assumption concerning the yield function ϕ and the evolution equations is made.*

Remark 4. *A second assumption frequently made is that the localization zone is introduced only at the end of a loading step, i.e. with delay (see, e.g. [12, 25]). To justify this approach, it is argued that the orientation of the singular surface $\partial_{\mathrm{s}}\Omega$ during an iteration would correspond to a non-equilibrium state. Indeed, this is correct. However, incorporating $\partial_{\mathrm{s}}\Omega$ into the finite element undergoing localization with one time step delay, the topology of $\partial_{\mathrm{s}}\Omega$ is computed by*

means of a trial-state (the respective finite element is purely elastic, resp. not localized, up to this time) which is a physically nonrelevant state. In the algorithmic formulation presented, the orientation of $\partial_{\mathrm{s}}\Omega$ is allowed to rotate in the first loading cycle (only in this cycle). According to computational plasticity, the topology of $\partial_{\mathrm{s}}\Omega$, corresponding to the first converged loading step (on global level), is stored and kept fixed.

Remark 5. *The numerical implementation is often based on explicit or partially explicit algorithms. More precisely, the direction of the displacement discontinuity is assumed to be constant within a particular increment (see, e.g. [15, 39]). Hence, in this case, the integration algorithm reduces to a single scalar valued equation. However, the drawbacks of explicit implementations are well known [28, 29]. Consequently, a fully implicit integration algorithm is proposed.*

Remark 6. *According to Equations (51) and (52) the linearizations have been computed with respect to $\overline{\boldsymbol{\sigma}}$, $\boldsymbol{q}$ and λ. However, ϕ, g and h are functions in $\overline{\boldsymbol{t}}$ (and in $\boldsymbol{q}$). Since $\overline{\boldsymbol{t}} = \boldsymbol{N} \cdot \overline{\boldsymbol{\sigma}}$, the partial derivative of an arbitrary function $\boldsymbol{f}$ in $\overline{\boldsymbol{t}}$ with respect to $\overline{\boldsymbol{\sigma}}$ is computed by applying the chain rule as $\partial_{\overline{\boldsymbol{\sigma}}} \boldsymbol{f} = (\boldsymbol{N} \otimes \partial_{\overline{\boldsymbol{t}}} \boldsymbol{f})^{\mathrm{sym}}$. By choosing $\overline{\boldsymbol{\sigma}}$ instead of $\overline{\boldsymbol{t}}$ as the independent variable, the proposed numerical framework is formally identical to the classical return-mapping algorithm.*

Remark 7. *Note that $\overline{\boldsymbol{\sigma}^{\mathrm{tr}}_{n+1}}$ is, in general, not coaxial to $\overline{\Delta\tilde{\boldsymbol{\varepsilon}}_{n+1}}$. Hence, the presented return-mapping algorithm has to be performed in global axes.*

4.3 Linearization of the stresses

Next, the linearization of the stresses necessary for an asymptotic quadratical convergence is computed. From Equation $(41)_1$, the change of the (local) stresses $\boldsymbol{\sigma}$ at $\boldsymbol{X}_i$ is obtained as

$$\mathrm{d}\boldsymbol{\sigma}_{n+1}(\boldsymbol{X}_i) = \mathbb{C} : \mathrm{d}\boldsymbol{\nabla}^{\mathrm{sym}} \bar{\boldsymbol{u}}_{n+1}(\boldsymbol{X}_i) - \mathbb{C} : \mathrm{d}\tilde{\boldsymbol{\varepsilon}}_{n+1}(\boldsymbol{X}_i). \tag{58}$$

Since a converged load step is characterized by

$$\mathrm{d}\tilde{\boldsymbol{\varepsilon}}_{n+1}(\boldsymbol{X}_i) = \mathrm{d}\left[\Delta\lambda_{n+1} \left(\partial_{\overline{\boldsymbol{t}}} g\Big|_{n+1} \otimes \boldsymbol{\nabla}\varphi(\boldsymbol{X}_i)\right)^{\mathrm{sym}}\right], \tag{59}$$

(see [28, 29]), Equation (58) results in

$$\begin{aligned}
\mathrm{d}\boldsymbol{\sigma}_{n+1}(\boldsymbol{X}_i) = \quad & \mathbb{C} : \mathrm{d}\boldsymbol{\nabla}^{\mathrm{sym}} \bar{\boldsymbol{u}}_{n+1}(\boldsymbol{X}_i) \\
- \quad & \Delta\lambda_{n+1}\, \mathbb{C} : \left(\partial^2_{\overline{\boldsymbol{t}} \otimes \overline{\boldsymbol{\sigma}}} g\Big|_{n+1} \otimes \boldsymbol{\nabla}\varphi(\boldsymbol{X}_i)\right)^{\mathrm{sym}} : \mathrm{d}\overline{\boldsymbol{\sigma}_{n+1}} \\
- \quad & \Delta\lambda_{n+1}\, \mathbb{C} : \left(\partial^2_{\overline{\boldsymbol{t}} \otimes \boldsymbol{q}} g\Big|_{n+1} \otimes \boldsymbol{\nabla}\varphi(\boldsymbol{X}_i)\right)^{\mathrm{sym}} \cdot \mathrm{d}\boldsymbol{q}_{n+1} \\
- \quad & \mathbb{C} : \left(\partial_{\overline{\boldsymbol{t}}} g\Big|_{n+1} \otimes \boldsymbol{\nabla}\varphi(\boldsymbol{X}_i)\right)^{\mathrm{sym}} \mathrm{d}\Delta\lambda_{n+1}.
\end{aligned} \tag{60}$$

Note that $\tilde{\boldsymbol{\varepsilon}}$ depends on $\overline{\boldsymbol{\sigma}}$ (and not on the local stresses $\boldsymbol{\sigma}$). Hence, the linearization of $\tilde{\boldsymbol{\varepsilon}}$ with respect to $\overline{\boldsymbol{\sigma}}$ is required. Analogously to Equation (51), the simple and double contractions in Equation (60) are not the standard ones (see also Equation (53)).

According to Equation (60), the linearization of $\boldsymbol{\sigma}$ depends on the linearizations of $\boldsymbol{\nabla}^{\mathrm{sym}} \bar{\boldsymbol{u}}$, $\overline{\boldsymbol{\sigma}}$, $\boldsymbol{q}$ and $\Delta\lambda$. Since in finite element analyses $\bar{\boldsymbol{u}}$ represents, in general, the driving variable, the linearizations $\mathrm{d}\overline{\boldsymbol{\sigma}}$, $\mathrm{d}\boldsymbol{q}$ and $\mathrm{d}\Delta\lambda$ have to be computed in terms of $\mathrm{d}\bar{\boldsymbol{u}}$ (see [28, 29]). For that purpose, the consistency condition associated with a converged load step, i.e. $\phi_{n+1} = 0$, is considered. The linearized counterpart of Equation $(49)_2$ reads

$$\mathrm{d}\phi_{n+1} = \partial_{\overline{\boldsymbol{\sigma}}} \phi_{n+1} : \mathrm{d}\overline{\boldsymbol{\sigma}_{n+1}} + \partial_{\boldsymbol{q}} \phi_{n+1} \cdot \mathrm{d}\boldsymbol{q}_{n+1} = 0. \tag{61}$$

Using Equation $(41)_1$, the linearization of the (average) stresses $\overline{\boldsymbol{\sigma}}$ is obtained as

$$\mathrm{d}\overline{\boldsymbol{\sigma}}_{n+1} = \mathbb{C} : \left(\mathrm{d}\overline{\boldsymbol{\nabla}^{\mathrm{sym}}\bar{\boldsymbol{u}}} - \mathrm{d}\bar{\tilde{\boldsymbol{\varepsilon}}}\right)\Big|_{n+1}. \tag{62}$$

Analogously to the local counterpart (59), a converged load step is characterized by

$$\mathrm{d}\overline{\tilde{\boldsymbol{\varepsilon}}_{n+1}} = \mathrm{d}\left[\Delta\lambda\ \left(\partial_{\overline{\boldsymbol{t}}} g \otimes \overline{\boldsymbol{\nabla}\varphi}\right)^{\mathrm{sym}}\right]\Big|_{n+1}. \tag{63}$$

Consequently, Equation (62) results in

$$\begin{aligned}\mathrm{d}\overline{\boldsymbol{\sigma}_{n+1}} = \boldsymbol{\Xi}_{n+1} : \big[\mathrm{d}\overline{\boldsymbol{\nabla}^{\mathrm{sym}}\bar{\boldsymbol{u}}} - \Delta\lambda\ \left(\partial^2_{\overline{\boldsymbol{t}}\otimes\boldsymbol{q}} g \otimes \overline{\boldsymbol{\nabla}\varphi}\right)^{\mathrm{sym}} \cdot \mathrm{d}\boldsymbol{q} \\ - \mathrm{d}\Delta\lambda\ \left(\partial_{\overline{\boldsymbol{t}}} g \otimes \overline{\boldsymbol{\nabla}\varphi}\right)^{\mathrm{sym}}\big]\Big|_{n+1},\end{aligned} \tag{64}$$

where the inverse of the algorithmic moduli $\boldsymbol{\Xi}$

$$\boldsymbol{\Xi}^{-1}_{n+1} := \mathbb{C}^{-1} + \Delta\lambda\ \left(\partial^2_{\overline{\boldsymbol{t}}\otimes\overline{\boldsymbol{\sigma}}} g \otimes \overline{\boldsymbol{\nabla}\varphi}\right)^{\mathrm{sym}}\Big|_{n+1} \tag{65}$$

has been introduced. Similarly, the linearizations of $\boldsymbol{q}$ are computed as

$$\mathrm{d}\boldsymbol{q}_{n+1} = \left(\boldsymbol{H}^{-1} + \Delta\lambda\ \partial^2_{\boldsymbol{q}\otimes\boldsymbol{q}} h\right)^{-1}\Big|_{n+1} \cdot \left(-\mathrm{d}\Delta\lambda\ \partial_{\boldsymbol{q}} h - \Delta\lambda\ \partial^2_{\boldsymbol{q}\otimes\overline{\boldsymbol{\sigma}}} h : \mathrm{d}\overline{\boldsymbol{\sigma}}\right)\Big|_{n+1}. \tag{66}$$

With Definitions (54) and $(56)_2$, the linearizations (64) and (66) are summarized in matrix notation according to

$$\boldsymbol{\Delta} = \boldsymbol{A}\ \left(\begin{bmatrix} \mathrm{d}\overline{\boldsymbol{\nabla}^{\mathrm{sym}}\bar{\boldsymbol{u}}} \\ \boldsymbol{0} \end{bmatrix} - \mathrm{d}\Delta\lambda\boldsymbol{\nabla}M\right)\Big|_{n+1}. \tag{67}$$

Inserting Equation (67) into Equation (61), the linearization of $\Delta\lambda$ is obtained as

$$\mathrm{d}\Delta\lambda_{n+1} = \frac{\left\{\boldsymbol{\nabla}\phi^T\ \boldsymbol{A}\ \begin{bmatrix} \mathrm{d}\overline{\boldsymbol{\nabla}^{\mathrm{sym}}\bar{\boldsymbol{u}}} \\ \boldsymbol{0} \end{bmatrix}\right\}\Big|_{n+1}}{\{\boldsymbol{\nabla}\phi^T\ \boldsymbol{A}\ \boldsymbol{\nabla}M\}|_{n+1}}. \tag{68}$$

Clearly, Equation (68) is formally identical to its counterpart appearing in the classical return-mapping algorithm (see [28, 29]).

Next, the linearizations of $\overline{\boldsymbol{\sigma}}$ and $\boldsymbol{q}$ with respect to $\mathrm{d}\boldsymbol{\nabla}^{\mathrm{sym}}\bar{\boldsymbol{u}}$ (resp. $\mathrm{d}\overline{\boldsymbol{\nabla}^{\mathrm{sym}}\bar{\boldsymbol{u}}}$) are computed. Combining Equations (68) and (67), the desired linearizations are computed as

$$\mathrm{d}\overline{\boldsymbol{\sigma}_{n+1}} = \overline{\mathbb{C}^{\mathrm{ep}}_{n+1}} : \mathrm{d}\overline{\boldsymbol{\nabla}^{\mathrm{sym}}\bar{\boldsymbol{u}}_{n+1}}, \tag{69}$$

with

$$\overline{\mathbb{C}^{\mathrm{ep}}_{n+1}} := \frac{\mathrm{d}\overline{\boldsymbol{\sigma}}}{\mathrm{d}\overline{\boldsymbol{\nabla}^{\mathrm{sym}}\bar{\boldsymbol{u}}}}\Big|_{n+1} = \boldsymbol{A}_{[11]} - \frac{\{\boldsymbol{A}\ \boldsymbol{\nabla}M \otimes \boldsymbol{\nabla}\phi^T\ \boldsymbol{A}\}_{[11]}}{\boldsymbol{\nabla}\phi^T\ \boldsymbol{A}\ \boldsymbol{\nabla}M}, \tag{70}$$

and

$$\mathrm{d}\boldsymbol{q}_{n+1} = \tilde{\boldsymbol{H}}_{n+1} \cdot \mathrm{d}\overline{\boldsymbol{\nabla}^{\mathrm{sym}}\bar{\boldsymbol{u}}_{n+1}}, \tag{71}$$

with

$$\tilde{\boldsymbol{H}}_{n+1} := \frac{\mathrm{d}\boldsymbol{q}}{\mathrm{d}\overline{\boldsymbol{\nabla}^{\mathrm{sym}}\bar{\boldsymbol{u}}}}\Big|_{n+1} = \boldsymbol{A}_{[21]} - \frac{\{\boldsymbol{A}\ \boldsymbol{\nabla}M \otimes \boldsymbol{\nabla}\phi^T\ \boldsymbol{A}\}_{[21]}}{\boldsymbol{\nabla}\phi^T\ \boldsymbol{A}\ \boldsymbol{\nabla}M}, \tag{72}$$

respectively. In Equations (70) and (72), the abbreviation $[\bullet]_{ij}$ indicating the submatrix ij has been used. Using Equations (68) and (69)–(72), the linearization (60) results in

$$\mathrm{d}\boldsymbol{\sigma}_{n+1}(\boldsymbol{X}_i) = \mathbb{C} : \mathrm{d}\boldsymbol{\nabla}^{\mathrm{sym}}\bar{\boldsymbol{u}}_{n+1}(\boldsymbol{X}_i) - \mathbb{B}_{n+1}(\boldsymbol{X}_i) : \mathrm{d}\overline{\boldsymbol{\nabla}^{\mathrm{sym}}\bar{\boldsymbol{u}}_{n+1}}, \tag{73}$$

with

$$\begin{aligned} \mathbb{B}_{n+1}(\boldsymbol{X}_i) = \quad & \Delta\lambda_{n+1}\, \mathbb{C} : \left(\partial^2_{\overline{\boldsymbol{t}}\otimes\overline{\boldsymbol{\sigma}}} g \Big|_{n+1} \otimes \boldsymbol{\nabla}\varphi(\boldsymbol{X}_i) \right)^{\mathrm{sym}} : \overline{\mathbb{C}^{\mathrm{ep}}_{n+1}} \\ - \quad & \Delta\lambda_{n+1}\, \mathbb{C} : \left(\partial^2_{\overline{\boldsymbol{t}}\otimes\boldsymbol{q}} g \Big|_{n+1} \otimes \boldsymbol{\nabla}\varphi(\boldsymbol{X}_i) \right)^{\mathrm{sym}} \cdot \tilde{\boldsymbol{H}}_{n+1} \\ - \quad & \mathbb{C} : \left(\partial_{\overline{\boldsymbol{t}}} g \Big|_{n+1} \otimes \boldsymbol{\nabla}\varphi(\boldsymbol{X}_i) \right)^{\mathrm{sym}} \otimes \frac{\{\boldsymbol{\nabla}\phi^T\, \boldsymbol{A}\}_{[1]}}{\boldsymbol{\nabla}\phi^T\, \boldsymbol{A}\, \boldsymbol{\nabla} M}. \end{aligned} \tag{74}$$

As mentioned before, some of the simple and double contractions in Equation (74) are not the standard ones. However, in the opinion of the author, confusion is excluded. Using VOIGT notation (the conversion between a tensor $\boldsymbol{A}$ and its corresponding matrix is indicated by brackets, i.e. $[\boldsymbol{A}]$) and introducing the so-called $\boldsymbol{B}$-operator via

$$\bar{\boldsymbol{u}} \approx \sum_{i=1}^{n_{\mathrm{node}}} N_i\, \bar{\boldsymbol{u}}^{\mathrm{e}}_i \quad \Rightarrow \quad [\boldsymbol{\nabla}^{\mathrm{sym}}\bar{\boldsymbol{u}}] = \boldsymbol{B}\, \bar{\boldsymbol{u}}^{\mathrm{e}}, \quad \text{with} \quad \bar{\boldsymbol{u}}^{\mathrm{e}^T} = [\bar{\boldsymbol{u}}^{\mathrm{e}}_1, \ldots, \bar{\boldsymbol{u}}^{\mathrm{e}}_{n_{\mathrm{node}}}], \tag{75}$$

Equation (73) is rewritten as

$$[\mathrm{d}\boldsymbol{\sigma}_{n+1}(\boldsymbol{X}_i)] = [\mathbb{C}]\; \boldsymbol{B}\mathrm{d}\bar{\boldsymbol{u}}^{\mathrm{e}}_{n+1} - [\mathbb{B}_{n+1}(\boldsymbol{X}_i)]\; \overline{\boldsymbol{B}}\mathrm{d}\bar{\boldsymbol{u}}^{\mathrm{e}}_{n+1}. \tag{76}$$

In contrast to classical continuum theories, the linearization of $\boldsymbol{\sigma}$ at a point $\boldsymbol{X}_i$ depends on the local strains ($\boldsymbol{B}\mathrm{d}\bar{\boldsymbol{u}}^{\mathrm{e}}$) but also on the average strains ($\overline{\boldsymbol{B}}\mathrm{d}\bar{\boldsymbol{u}}^{\mathrm{e}}$). This results directly from the weak form of traction continuity.

Remark 8. *The presented numerical implementation holds for a broad range of different constitutive equations describing the inelastic behavior of the considered material. For a* VON MISES*-type plasticity model, the proposed algorithmic formulation is specified in Appendix A and B.*

Remark 9. *The vector $\boldsymbol{N}$ defining the orientation of the localization surface has to be computed. For that purpose, different concepts can be applied such as non-classical bifurcation analyses (see [4, 12, 41]) and stress-based criteria [7]. The specific criteria applied in the numerical studies presented in Section 5 are described in Subsection 5.1 and Subsection 5.2, respectively.*

5 NUMERICAL EXAMPLES

The applicability of the novel algorithmic formulation and its numerical performance are investigated by means of a two-dimensional re-analysis of the simple shear test (Subsection 5.1), a finite element analysis of the extension of a strip with a circular hole (Subsection 5.3) as well as by means of a fully three-dimensional analysis of shear band formation occurring in a steel made bar (Subsection 5.2).

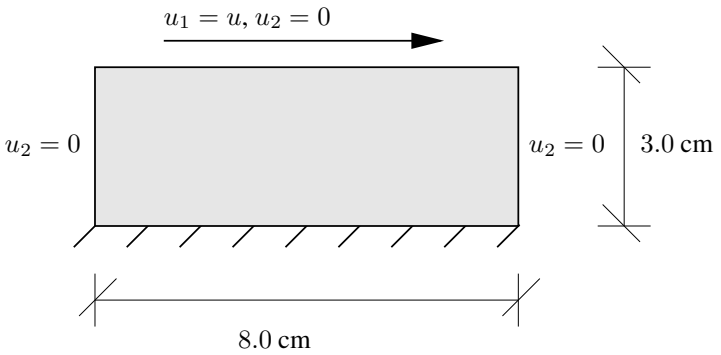

material parameters

E	= 20690	[kN/cm^2]
ν	= 0.29	
σ_{y}	= 45	[kN/cm^2]
H	= 200	[kN/cm^3]

Figure 2: Numerical study of the simple shear test: Dimensions (in [cm]) and material parameters; thickness t of the slab $t = 1$ cm.

5.1 Simple shear test

This subsection contains a numerical re-analysis of the simple shear test. The geometry, the loading and boundary conditions of the steel made block are illustrated in Figure 2 (see also [13]). For the modeling of slip bands in ductile materials, a VON MISES-type yield function is adopted. Restricting attention to plane stress conditions, this function is written as

$$\phi = |\boldsymbol{t} \cdot \boldsymbol{m}| - q(\alpha), \tag{77}$$

where $\boldsymbol{m}$ represents a unit vector orthogonal to $\boldsymbol{N}$. Applying the principle of maximum dissipation, the evolution equations of the displacement discontinuity and the internal variable are well-defined. The resulting constitutive model is summarized in Appendix B. The traction-separation law is completed by a linear softening function of the type

$$q(\alpha) = \sigma_{\mathrm{y}} - H\ \alpha. \tag{78}$$

Since for the specific constitutive model $\dot{\alpha} = \lambda = ||\ [\![\dot{\boldsymbol{u}}]\!]\ ||_2$ holds (see Appendix B), the amplitude of the displacement discontinuity associated with a completely softened material, i.e. $q = 0$, is obtained as $\alpha_{\max} = \sigma_{\mathrm{y}}/H$.

According to Equation (19), the stresses in $\Omega^{\pm}$ are computed from the 4th-order tensor $\mathbb{C}$. Here, HOOKE's law characterized by

$$\mathbb{C} = \frac{E}{1+\nu}\ \mathbb{I}^{\mathrm{sym}} + \frac{E\ \nu}{1-\nu^2}\ \boldsymbol{1} \otimes \boldsymbol{1} \tag{79}$$

is adopted. In Equation (79), $\mathbb{I}^{\mathrm{sym}}$ denotes the symmetric 4th-order unit tensor, i.e. $\boldsymbol{A}^{\mathrm{sym}} = \mathbb{I}^{\mathrm{sym}} : \boldsymbol{A}$, for every second-order tensor $\boldsymbol{A}$. As a consequence, the resulting stress field corresponding to a purely elastic deformation is computed analytically as (see Figure 2)

$$\boldsymbol{\sigma} = \sigma_{12}\ \left(\boldsymbol{e}_1 \otimes \boldsymbol{e}_2 + \boldsymbol{e}_2 \otimes \boldsymbol{e}_1\right), \quad \text{with} \quad \sigma_{12} = \frac{E}{2\ (1+\nu)}\ \frac{u}{3.0}, \tag{80}$$

where $\boldsymbol{e}_i$ denotes the standard CARTESIAN bases. As mentioned in [15, 33], for the case of simple shearing of VON MISES-type solids, material bifurcation, i.e. the formation of strong discontinuities, occurs at the onset of yielding and the respective shear band is horizontally oriented ($\boldsymbol{N} = \boldsymbol{e}_2$ and $\boldsymbol{m} = \boldsymbol{e}_1$). Inserting these conditions, together with Equation (80), into Equation (77), leads to

$$\left.\begin{array}{l} \phi = 0 \\ q = \sigma_{\mathrm{y}} \end{array}\right\} \quad \Rightarrow \quad u_{\mathrm{y}} = 6.0\ \sigma_{\mathrm{y}}\ \frac{1+\nu}{E}. \tag{81}$$

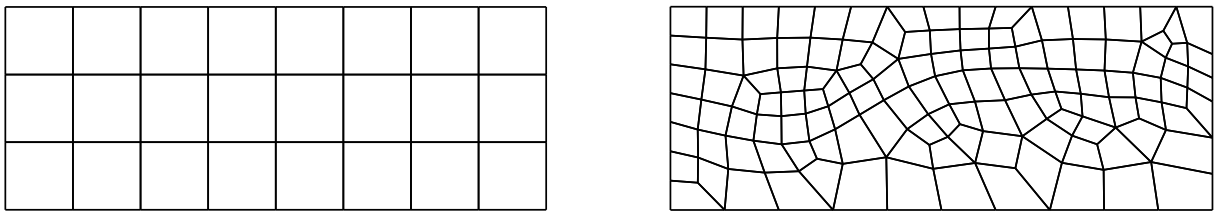

a) structured mesh b) unstructured mesh

Figure 3: Numerical study of the simple shear test: Finite element discretizations.

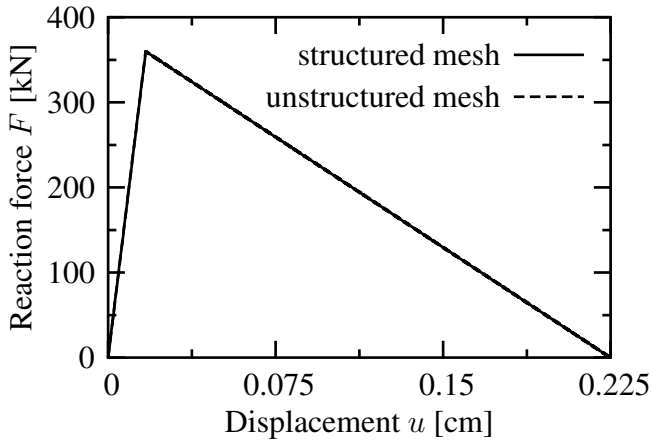

Figure 4: Numerical study of the simple shear test: Load-displacement diagrams obtained from the structured and the unstructured mesh.

Hence, a slip band associated with a global softening response starts to form at a horizontal displacement of $u_{\mathrm{y}} = 1.6834 \cdot 10^{-2}$ cm.

For the assessment of mesh dependence of the results computed numerically, two different finite element discretizations are used. The displacement controlled analysis is performed by means of one structured mesh (24 4-node plane stress elements), i.e. the edges of the elements are aligned with the topology of the analytical solution of $\partial_{\mathrm{s}}\Omega$, and one unstructured mesh containing 119 4-node plane stress elements (see Figure 3). For the case of plane stress conditions, the numerical implementation of the VON MISES-type traction-separation law is summarized in Appendix B. The orientation of $\partial_{\mathrm{s}}\Omega$, i.e. $\boldsymbol{N}$, is computed from a bifurcation analysis according to [4]. However, for the simple shear test, two possible solutions are obtained. Uniqueness is achieved by applying the principle of maximum dissipation to the set of admissible candidates. Hence, the localization surface which maximizes the dissipation is used. For further details, refer to [41].

The numerical analyses are performed with enforcing slip band path continuity. For that purpose, the following algorithm is applied: When localization is detected, the normal vector $\boldsymbol{N}$ of a new slip band is computed first. If no neighboring finite elements are localized, $\partial_{\mathrm{s}}\Omega$ is assumed to cross the centroid of the respective element. On the other side, if a slip band has already formed in one of the neighboring elements, the new band $\partial_{\mathrm{s}}\Omega$ is connected with the existing one. It should be mentioned again that the discontinuous displacement field is modeled in an incompatible fashion. Hence, the enforcement of a continuous slip band path does not guarantee that the displacement jump itself is continuous across the edge of two neighboring finite elements. Localization is induced by weakening the initial yield stress of one element about 0.4%.

In Figure 4, the load-displacement diagrams obtained from the numerical analyses of the structured and the unstructured discretization are illustrated. From the investigated finite ele-

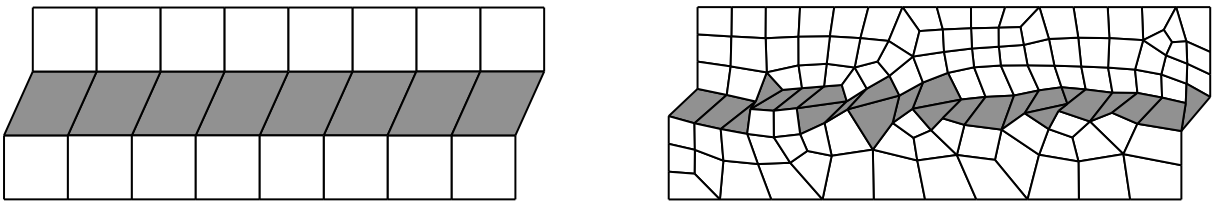

a) structured mesh b) unstructured mesh

Figure 5: Numerical study of the simple shear test: Distribution of the internal variable α representing the relative shear sliding displacement obtained from the structured and the unstructured mesh (2-fold magnification of the displacements).

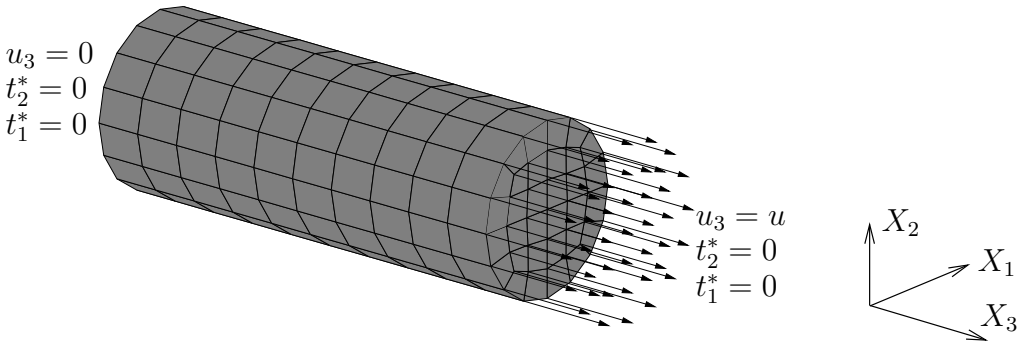

Figure 6: Numerical study of the tension test: Finite element discretization (320 8-node brick elements) and boundary conditions; geometry of the circular bar: length $l = 8$ cm, radius $r = 1.5$ cm; material parameters according to Figure 2.

ment discretizations a maximum loading of 360 kN ($= 8.0\ \sigma_{\mathrm{y}}$) at $u = u_{\mathrm{y}}$ is obtained. The horizontal displacement at the top of the steel made block corresponding to a completely softened material is predicted as $\alpha_{\max} = 0.225$ cm. That is, the numerical results associated with both discretizations are identical to one another and agree with the analytical solution.

The resulting inelastic deformations represented by means of the internal variable α corresponding to the final stage of deformation are shown in Figure 5. According to Figure 5, both meshes predict a horizontally oriented shear band. That is, the geometry of the localization surface computed numerically is independent of the respective spatial discretization and is identical to that of the analytical solution.

5.2 Shear band formation in a circular bar

In this subsection, the finite element formulation as proposed in Section 4 is employed for a fully three-dimensional numerical analysis of a shear band formation occurring in a steel made circular bar. The support conditions of the circular bar (radius $r = 1.5$ cm, length $l = 8$ cm), are illustrated in Figure 6. Following Subsection 5.1, shear band formation is modeled by means of a VON MISES-type traction-separation law. According to Appendix A, the generalization of the plane stress constitutive law (77) reads

$$\phi = ||\boldsymbol{t}_m||_2 - q(\alpha), \quad \text{with} \quad \boldsymbol{t}_m := \boldsymbol{t} - (\boldsymbol{t} \cdot \boldsymbol{N})\, \boldsymbol{N}. \tag{82}$$

For more details, refer to Appendix A. Analogously to Subsection 5.1, a linear softening evolution of the type (78) is assumed. The evolution equations of the displacement discontinuity and the internal variable are derived from the principle of maximum dissipation. The resulting constitutive model is summarized in Appendix A.

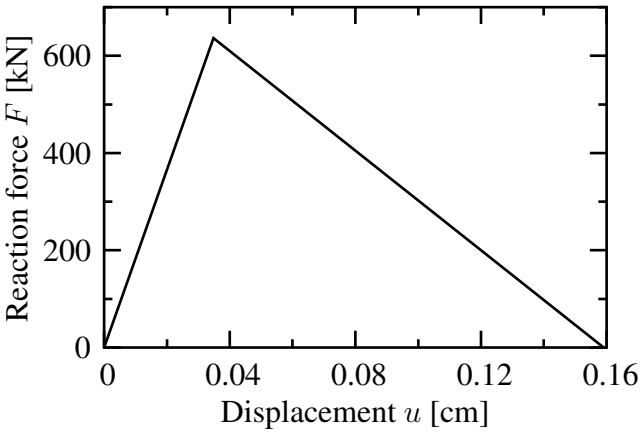

Figure 7: Numerical study of the tension test: Analytically computed load-displacement diagram.

In the elastic domain, the prescribed displacement field (displacement controlled analysis) characterized by u, leads to the stress tensor

$$\boldsymbol{\sigma} = u \, \frac{E}{8.0} \, \boldsymbol{e}_3 \otimes \boldsymbol{e}_3. \tag{83}$$

It is well known (see e.g. [4, 33]), that the angle between the normal $\boldsymbol{N}$ of a possible slip band and the direction of the major principle stress is about 45° (in the case of VON MISES-plasticity). However, since the stress state characterized by Equation (83) is rotationally symmetric with respect to the major principle stress direction ($\boldsymbol{e}_3$), an infinite number of admissible solutions exists. Without loss of generality, $\boldsymbol{N}^T = [0; 1/\sqrt{2}; 1/\sqrt{2}]$ is chosen. In contrast to Subsection 5.1, the shear band is assumed to propagate when the condition $\phi_{n+1} > 0$ is fulfilled (i.e. a loading step). Before this inequality is satisfied for the first time, purely elastic deformations are postulated. Consequently, by inserting $\boldsymbol{N}^T = [0; 1/\sqrt{2}; 1/\sqrt{2}]$, together with the stress tensor (83), into Equation $(82)_2$, leads to

$$\boldsymbol{t}_m^T = \left[0; \frac{1}{2\sqrt{2}}; \frac{1}{2\sqrt{2}}\right] \, \sigma_{33} \quad \Longrightarrow \quad ||\boldsymbol{t}_m||_2 = \frac{1}{2} \, u \, \frac{E}{8.0}. \tag{84}$$

Hence, the slip band starts to develop at $u_{\mathrm{y}} = 16.0/E \; \sigma_{\mathrm{y}}$ and the direction of the displacement discontinuity is obtained as $[\![\boldsymbol{u}]\!]^T \, / || \, [\![\boldsymbol{u}]\!] \, ||_2 = [0; -1/\sqrt{2}; 1/\sqrt{2}]$ (see Appendix A). According to Equation (78), the amplitude of the displacement discontinuity associated with a completely softened material, i.e. $q = 0$, is obtained as $\alpha_{\max} = \sigma_{\mathrm{y}}/H$. With the direction of the displacement discontinuity $[\![\boldsymbol{u}]\!]^T \, / || \, [\![\boldsymbol{u}]\!] \, ||_2 = [0; -1/\sqrt{2}; 1/\sqrt{2}]$, the maximum displacement $u_{\max}$ corresponding to a completely softened material is computed as $u_{\max} = 1/\sqrt{2} \; \alpha_{\max}$. Combining u_{y} and $u_{\max}$ (together with the stresses associated with these displacements), the resulting load-displacement diagram is defined (see Figure 7). Clearly, the assumed localization condition ($\phi_{n+1} > 0$) is not equivalent to the classical bifurcation analysis (see [4, 33]). However, as shown in Figure 7, the applied condition leads to a load-displacement diagram which can be described analytically in a closed form. Hence, it is well suitable for a comparison with the numerically computed results. Of course, other bifurcation conditions can be applied as well.

Following the previous subsection, the numerical analyses are performed with enforcing slip band path continuity. That is, if a slip band has already formed in one of the neighboring elements, the new band $\partial_{\mathrm{s}}\Omega$ is connected with the existing one. However, the extension of this band tracking algorithm to the fully three-dimensional case is, in general, not trivial. Since the

cut set of a planar localization surface $\partial_{\mathrm{s}}\Omega$ and one surface of a three-dimensional brick element is represented by a straight line, it is, in general, impossible to connect to neighboring slip bands in a continuous fashion (at this respective cut set). However, in the numerical analyses presented in this paragraph, the vector $\boldsymbol{N}$ computed within all elements varies only marginally. Hence, the just mentioned problem does never occur. For more complex geometries of the slip band, e.g. curved surfaces, alternative band tracking strategies such as that suggested in [42] have to be applied.

Localization is activated by weakening the initial yield stress σ_{y} of one element about 0.4%. In contrast to the two-dimensional case, the normal vector of the first localized element is explicitly prescribed as $\boldsymbol{N}^T = [0; 1/\sqrt{2}, 1/\sqrt{2}]$. As mentioned before, this is necessary, since an infinite number of possible solutions exists. For the assessment of the dependence of the prescribed normal vector of the first localized element on the numerical results, different orientations are considered. Starting with $\boldsymbol{N}^T = \boldsymbol{N}^{*T} := [0; 1/\sqrt{2}; 1/\sqrt{2}]$, the orientation of the slip band associated with the weakened element is varied according to

$$\boldsymbol{N} = \boldsymbol{T}(\theta)\ \boldsymbol{N}^* \tag{85}$$

with

$$\boldsymbol{T}(\theta) = \begin{bmatrix} \cos\theta & -\sin\theta & 0 \\ \sin\theta & \cos\theta & 0 \\ 0 & 0 & 1 \end{bmatrix}, \tag{86}$$

i.e. a rotation about the X_3 axis. 10 different finite element computations are performed. At first, θ is set to zero. Subsequently, this angle is increased up to 90° in steps of 10°.

Figure 8 contains the distribution of the internal variable α representing the relative shear sliding displacement at $\partial_{\mathrm{s}}\Omega$ obtained from the proposed finite element formulation. As expected, the computed deformation depends on the orientation of $\partial_{\mathrm{s}}\Omega$ and consequently, on θ. However, with the exception of a rotation about the X_3 axis (see Figure 6), the numerical results are independent of θ. For each analysis, a plane shear band $\partial_{\mathrm{s}}\Omega$ is obtained. In agreement with the analytical solution, the angle between the normal $\boldsymbol{N}$ associated with this band and the direction of the major principle stress is about 45°. It should be noted that the surfaces of the finite elements are not aligned with the singular hyperplane $\partial_{\mathrm{s}}\Omega$. Hence, the discretization illustrated in Figures 6 and 8 is unstructured with respect to $\partial_{\mathrm{s}}\Omega$.

The resulting load-displacement diagrams are shown in Figure 9. As illustrated in Figure 9, the computed structural response is independent of θ. For all finite element analyses ($\theta = 0^\circ$ to $\theta = 90^\circ$), the obtained load-displacement diagram is identical to the analytical solution (compare Figure 9 to Figure 7).

5.3 Extension of a strip with a circular hole

This subsection contains a numerical analysis of the extension of a steel made strip with a circular hole (see Figure 10). A similar problem has been investigated numerically by several authors, see e.g. [28]. As in the previous subsections, for the modeling of slip bands in ductile materials, the VON MISES yield function according to Equation (77) is adopted. Analogously to the previous subsection, the shear band is assumed to propagate when the condition $\phi > 0$ (a loading step) is fulfilled. In contrast to the simple shear test and the uniaxial tensile test as presented in Subsections 5.1 and 5.2, the stress state in the strip is highly nonhomogeneous even before localization is activated.

To demonstrate the independence of the numerically computed results on the spatial discretization, three different finite element meshes are used. According to Figure 11, mesh I and

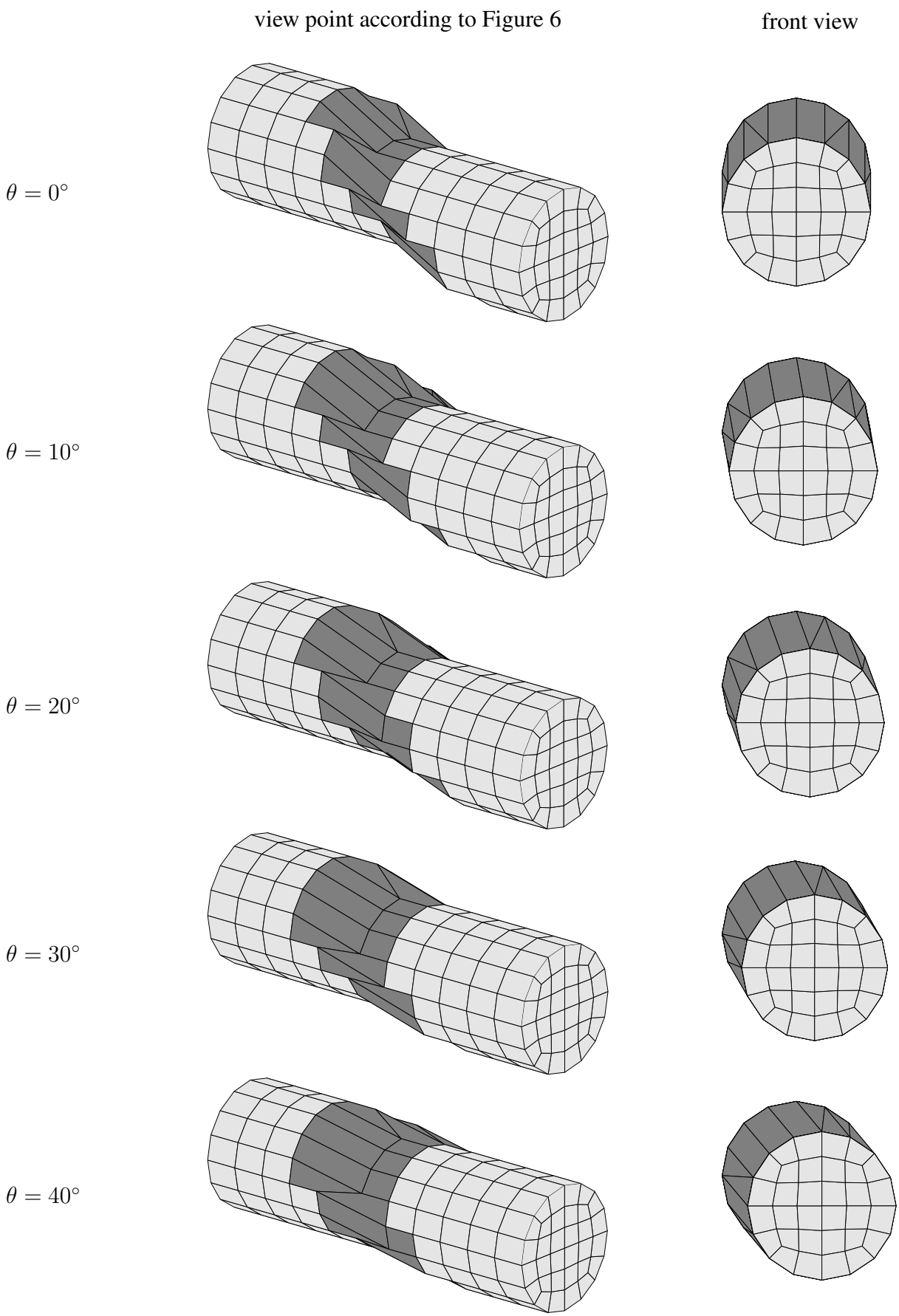

Figure 8: Numerical study of the tension test: Distribution of the internal variable α representing the relative shear sliding displacement obtained from the proposed finite element formulation (5-fold magnification of the displacements); solutions corresponding to $\theta = 50^\circ$ to $\theta = 90^\circ$ are not shown.

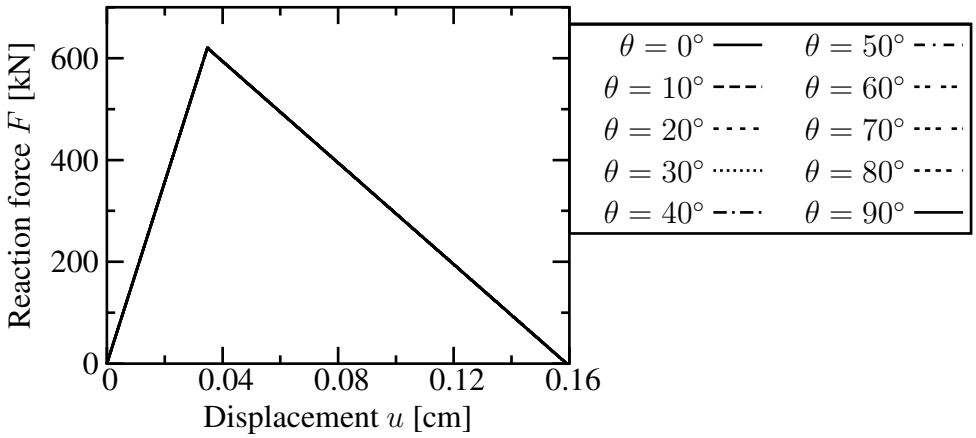

Figure 9: Numerical study of the tension test: Load-displacement diagram obtained from the proposed algorithmic formulation.

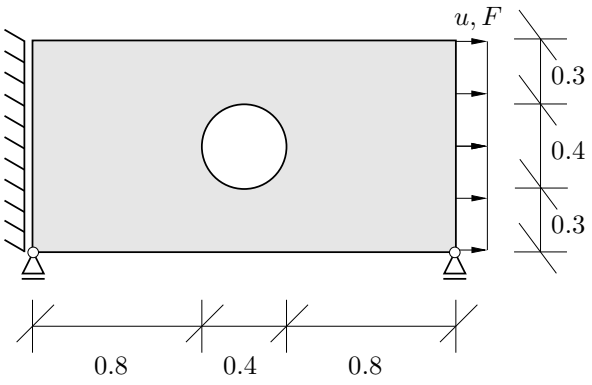

material parameters

E	= 20690	[kN/cm^2]
ν	= 0.29	
σ_y	= 45	[kN/cm^2]
H	= 4000	[kN/cm^3]

Figure 10: Numerical study of the extension of a strip with a circular hole: Dimensions (in [cm]) and material parameters; thickness of the strip $t = 0.1$ cm.

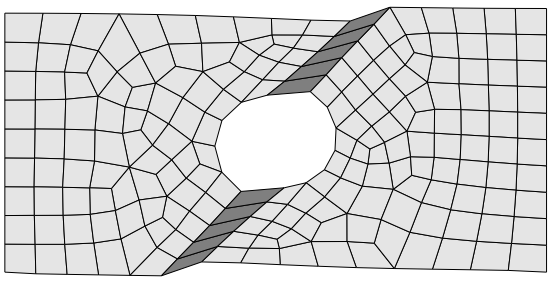

mesh I

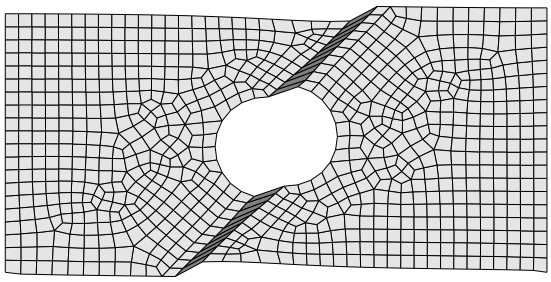

mesh II

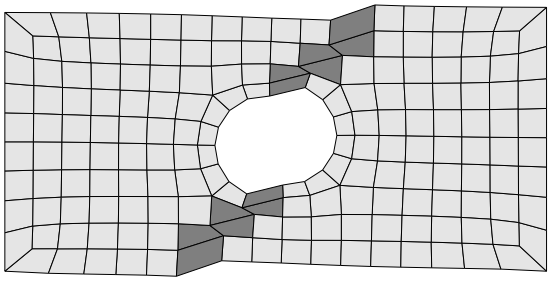

mesh III

Figure 11: Numerical study of the extension of a strip with a circular hole: Distribution of the internal variable α representing the relative shear sliding displacement as obtained from discretizations mesh I-III (8-fold magnifications of displacements).

mesh II are aligned with the slip band path expected. They contain 192 and 834 4-node plane stress elements, respectively. In addition to these meshes, an unstructured discretization (mesh III) is considered as well. It has been designed automatically by applying an overlay procedure and consists of 176 elements. It should be noted that in contrast to the problems analyzed in the previous subsections, the stress field associated with the problem illustrated in Figure 10 is highly inhomogeneous even in the elastic regime. As a consequence, no imperfections are nesessary to activate localization.

In Figure 11, the distribution of the internal variable α representing the relative shear sliding displacement obtained from the numerical analyses is illustrated. The plots are associated with a displacement u of magnitude $u = 0.008835$ cm. As expected, the slip bands computed are almost completely independent of the spatial discretization. The angle between these bands and the horizontal is about 45°. It should be noted that in Figure 11 only the primary slip bands are shown. Secondary bands, that is, those associated with a relative shear sliding displacement several orders of magnitude less than that of the primary localization surfaces are not presented.

Although the topology of the slip bands computed numerically can be estimated by means of Figure 11, a more precise analysis of the topology is not realizable. For a more detailed investigation, the primary localization surfaces are illustrated in Figure 12. As expected from Figure 11, the slip bands obtained from the finite element analyses based on mesh I-III are almost identical. They are nearly independent of the size of the finite elements and the bias induced by the discretization. However, according to Figure 12, the slip band orientations are not constant. They vary between $\theta \in [37.44^\circ, 47.55^\circ]$, $\theta \in [38.74^\circ - 49.71^\circ]$ and $\theta \in [38.67^\circ, 51.25^\circ]$ for meshes I, II and III, respectively. Here, θ denotes the angle between the slip band and the horizontal. The slip bands start to form at the hole under a relatively small angle θ. If the loading is further increased, these bands propagate. At the same time, the angle θ at the tip of the band increases. After reaching the maximum value, θ decreases in the vicinity of the upper and the lower boundary of the strip. That is, the slip bands computed numerically are slightly curved.

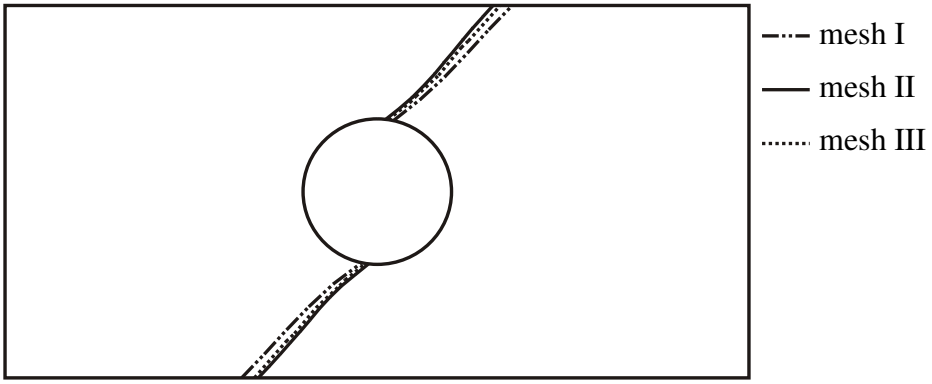

Figure 12: Numerical study of the extension of a strip with a circular hole: Topology of the primary slip band as computed from discretizations mesh I-III.

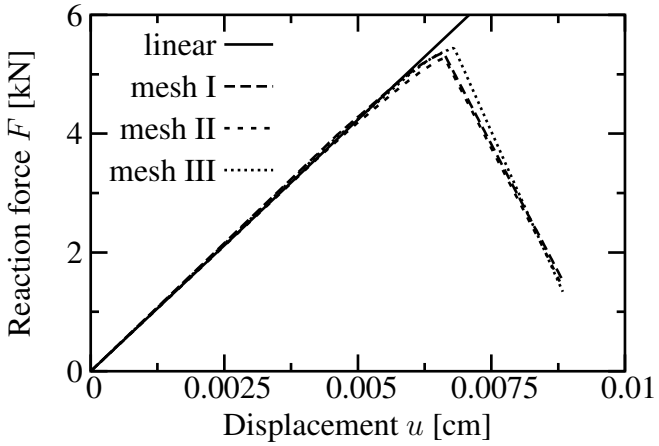

Figure 13: Numerical study of the extension of a strip with a circular hole: Load-displacement diagrams as computed from discretizations mesh I-III.

The load-displacement diagrams computed from the numerical analyses are shown in Figure 13. Each of the three discretizations predicts an almost identical structural response. According to Figure 13, a maximum loading of $F_{\max} = 5.36$ kN, $F_{\max} = 5.27$ kN and $F_{\max} = 5.44$ kN is obtained from meshes I-III. By comparing the load-displacement curves to that of the linear solution, it is seen that localization is activated significantly before the maximum loading $F_{\max}$ is reached. Not until the slip band separates the steel made strip completely, an overall softening response is observed. However, the differences of the post-peak behavior computed from meshes I-III are marginal.

6 CONCLUSION

A novel three-dimensional algorithmic framework for the numerical modeling of locally embedded strong discontinuities, suitable for the analysis of material failure, such as cracking in brittle structures or shear bands in soils, has been presented. In contrast to previous works on this subject, the proposed framework is applicable to any constitutive equation characterizing the inelastic part of deformations. Referring to the yield (failure) function and the evolution equations, no special assumption has to be made. Additionally, the suggested numerical implementation is not restricted to a particular type of finite element. Both in the two-dimensional and

three-dimensional case, arbitrary polynomial orders of the approximation of the displacement field can be accounted for.

Based on the weak form of traction equilibrium across a singular surface and the assumption of continuity of the traction vector, a constitutive law which is formally identical to classical stress-space based plasticity theory has been developed. Analogously to standard (local) continuum models, the respective material model is based on a yield (failure) function and some potentials defining the evolution of inelastic deformations. However, and in contrast to classical local plasticity theory, these functions are associated with the weak form of traction equilibrium across the singular surface and, consequently, they are formulated in terms of average stresses.

Since the constitutive equations of the proposed strong discontinuity model, describing the inelastic part of deformation, are formally identical to classical plasticity theory, the by now standard return-mapping algorithm has been applied to the numerical implementation. In contrast to the original implementation based on the static condensation technique, the presented finite element model only requires minor modifications of material subroutines designed for standard plasticity models. Despite the differences between the suggested numerical framework and the original implementation of the strong discontinuity approach, both finite element models are completely equivalent.

The applicability of the novel algorithmic formulation and its numerical performance have been investigated by means of two two-dimensional as well as by means of a fully three-dimensional numerical analysis of shear band formation. For that purpose, a VON MISES-type plasticity model has been incorporated into a 4-node plane stress element and into an 8-node brick element, respectively.

Acknowledgement

This work was completed under the financial support of the Deutsche Forschungsgemeinschaft (DFG) through project A4 under supervision of Prof. O.T. Bruhns within the Collaborative Research Centre 398. The author wishes to express his sincere gratitude to this support. Furthermore, the author would like to thank Prof. O.T. Bruhns for his helpful comments.

A Three-dimensional constitutive model for the analysis of shear band formation

This appendix is concerned with a brief summary of a three-dimensional material model suitable for the analysis of shear band formation. The two-dimensional counterpart is contained in Appendix B. The proposed constitutive equations are employed in the numerical analyses presented in Subsection 5.2.

In many cases, shear stresses are significantly involved in the formation of slip bands. Hence, it is convenient to consider the VON MISES yield criterion defined by

$$\phi = ||\mathrm{dev}[\boldsymbol{\sigma}]||_2 - q(\alpha) \leq 0, \quad \text{with} \quad \mathrm{dev}[\bullet] := (\bullet) - \frac{1}{3}\ [(\bullet) : \mathbf{1}]\ \mathbf{1}. \tag{87}$$

However, since the proposed numerical model is based on a traction-separation law, criterion (87) has to be modified. Starting with the decomposition

$$\boldsymbol{t} = \boldsymbol{t}_N + \boldsymbol{t}_m, \tag{88}$$

of the traction vector $\boldsymbol{t} = \boldsymbol{\sigma} \cdot \boldsymbol{N}$, acting on $\partial_{\mathrm{s}}\Omega$, into a normal component $\boldsymbol{t}_N$ and a shear component $\boldsymbol{t}_m$ via

$$\boldsymbol{t}_N = (\boldsymbol{t} \cdot \boldsymbol{N})\ \boldsymbol{N}, \qquad \boldsymbol{t}_m = \boldsymbol{t} - (\boldsymbol{t} \cdot \boldsymbol{N})\ \boldsymbol{N}, \tag{89}$$

criterion (87) is rewritten as

$$\phi = ||\boldsymbol{t}_m||_2 - q(\alpha([\![\boldsymbol{u}]\!])). \tag{90}$$

According to Equation $(89)_2$, $\boldsymbol{t}_m$ depends linearly on $\boldsymbol{t}$. Hence, introducing a third-order tensor $\mathcal{T}$, Equation $(89)_2$ yields

$$\boldsymbol{t}_m = \mathcal{T} : \boldsymbol{\sigma}, \quad \text{with} \quad \mathcal{T} := \boldsymbol{N} \cdot \mathbb{I}^{\text{sym}} - \boldsymbol{N} \otimes \boldsymbol{N} \otimes \boldsymbol{N}. \tag{91}$$

Applying Equation (91), Equation (90) leads to

$$\phi = ||\mathcal{T} : \boldsymbol{\sigma}||_2 - q(\alpha([\![\boldsymbol{u}]\!])). \tag{92}$$

With Equation (92), and following Section 3, the weak form of traction continuity associated with inelastic loading is obtained as

$$\phi = ||\mathcal{T} : \overline{\boldsymbol{\sigma}}||_2 - q(\alpha([\![\boldsymbol{u}]\!])) = 0. \tag{93}$$

Analogously to Section 4, the notation $\overline{(\bullet)} := 1/V \int_\Omega (\bullet) \mathrm{d}V$ has been used. From Equation (93), the assumption $\boldsymbol{\nabla}[\![\boldsymbol{u}]\!] = \boldsymbol{0}$ and the principle of maximum dissipation, the evolution equation

$$[\![\dot{\boldsymbol{u}}]\!] = \lambda \, \partial_{\overline{\boldsymbol{t}}} \phi \quad \text{with} \quad \partial_{\overline{\boldsymbol{t}}} \phi = \frac{\partial \phi}{\partial \overline{\boldsymbol{t}_m}} \cdot \frac{\partial \overline{\boldsymbol{t}_m}}{\partial \overline{\boldsymbol{t}}} \tag{94}$$

of the displacement discontinuity is derived. Using the projection $\boldsymbol{T}$ defined by

$$\boldsymbol{T} := \frac{\partial \overline{\boldsymbol{t}_m}}{\partial \overline{\boldsymbol{t}}} = \boldsymbol{1} - \boldsymbol{N} \otimes \boldsymbol{N} \quad \Rightarrow \quad \overline{\boldsymbol{t}_m} = \boldsymbol{T} \cdot \overline{\boldsymbol{t}} \tag{95}$$

and applying the identity $\overline{\boldsymbol{t}_m} = \boldsymbol{T} \cdot \overline{\boldsymbol{t}_m}$ to Equation (93), Equation $(94)_2$ yields

$$\partial_{\overline{\boldsymbol{t}}} \phi = \frac{\overline{\boldsymbol{t}_m}}{||\overline{\boldsymbol{t}_m}||_2}. \tag{96}$$

Consequently, the evolution equation of the displacement jump is obtained as

$$[\![\dot{\boldsymbol{u}}]\!] = \lambda \, \frac{\overline{\boldsymbol{t}_m}}{||\overline{\boldsymbol{t}_m}||_2}. \tag{97}$$

The model is completed by the evolution equation associated with the internal variable α. Assuming associativity, the rate of α results in

$$\dot{\alpha} = \lambda. \tag{98}$$

Adopting this specific constitutive model, several simplifications associated with the numerical implementation as presented in Section 4 can be accounted for. Since the second derivatives of the yield function, resp. the evolution equations, are characterized by

$$\partial^2_{q^2} h = \partial^2_{q^2} \phi = 0, \quad \partial^2_{q\overline{\boldsymbol{\sigma}}} h = \partial^2_{q\overline{\boldsymbol{\sigma}}} \phi = 0, \quad \partial^2_{\boldsymbol{t}_q} g = \partial^2_{\boldsymbol{t}_q} \phi = 0 \tag{99}$$

and

$$\partial^2_{\overline{\boldsymbol{t}} \otimes \overline{\boldsymbol{\sigma}}} g = \partial^2_{\overline{\boldsymbol{t}} \otimes \overline{\boldsymbol{\sigma}}} \phi = \frac{1}{||\overline{\boldsymbol{t}_m}||_2} \left(\mathcal{T} - \frac{\overline{\boldsymbol{t}_m}}{||\overline{\boldsymbol{t}_m}||_2} \otimes \frac{\overline{\boldsymbol{t}_m}}{||\overline{\boldsymbol{t}_m}||_2} \cdot \mathcal{T} \right), \tag{100}$$

respectively, the generalized moduli $\boldsymbol{A}$ (see Equation (54)) degenerate to a diagonal hypermatrix, i.e.

$$\boldsymbol{A} = \text{diag}\,(\boldsymbol{\Xi};\ H)|_{n+1}\,. \tag{101}$$

According to Equation (65), $\boldsymbol{\Xi}$ denotes the algorithmic moduli. Using Equation (100), linearization of the increment of the plastic multiplier, i.e. $\Delta\lambda_{n+1}$, corresponding to a converged state (see Equation (68)) results in

$$\mathrm{d}\Delta\lambda_{n+1} = \left.\frac{(\partial_{\overline{\boldsymbol{t}}}\phi \otimes \boldsymbol{N}) : \boldsymbol{\Xi} : \mathrm{d}\overline{\boldsymbol{\nabla}^{\mathrm{sym}}\bar{\boldsymbol{u}}_{n+1}}}{(\partial_{\overline{\boldsymbol{t}}}\phi \otimes \boldsymbol{N}) : \boldsymbol{\Xi} : (\partial_{\overline{\boldsymbol{t}}}\phi \otimes \overline{\boldsymbol{\nabla}\varphi}) - H}\right|_{n+1}, \tag{102}$$

and the 4th-order tensor $\overline{\mathbb{C}^{\mathrm{ep}}}$ (see Equation (70)) is computed as

$$\overline{\mathbb{C}^{\mathrm{ep}}_{n+1}} = \boldsymbol{\Xi}_{n+1} - \left.\frac{\boldsymbol{\Xi} : \left(\partial_{\overline{\boldsymbol{t}}} g \otimes \overline{\boldsymbol{\nabla}\varphi}\right) \otimes \left(\partial_{\overline{\boldsymbol{t}}}\phi \otimes \boldsymbol{N}\right) : \boldsymbol{\Xi}}{\left(\partial_{\overline{\boldsymbol{t}}}\phi \otimes \boldsymbol{N}\right) : \boldsymbol{\Xi} : \left(\partial_{\overline{\boldsymbol{t}}} g \otimes \overline{\boldsymbol{\nabla}\varphi}\right) - H}\right|_{n+1}. \tag{103}$$

With the identity

$$\frac{\{\boldsymbol{\nabla}\phi^T\ \boldsymbol{A}\}_{[1]}}{\boldsymbol{\nabla}\phi^T\ \boldsymbol{A}\ \boldsymbol{\nabla}M} = \left.\frac{\left(\partial_{\overline{\boldsymbol{t}}}\phi \otimes \boldsymbol{N}\right) : \boldsymbol{\Xi}}{\left(\partial_{\overline{\boldsymbol{t}}}\phi \otimes \boldsymbol{N}\right) : \boldsymbol{\Xi} : \left(\partial_{\overline{\boldsymbol{t}}} g \otimes \overline{\boldsymbol{\nabla}\varphi}\right) - H}\right|_{n+1}, \tag{104}$$

the tensor $\mathbb{B}$ (see Equation (73)) required for the linearization of the stresses is well-defined.

B Two-dimensional constitutive model for the analysis of shear band formation

This appendix contains the two-dimensional counterpart of the three-dimensional constitutive model as summarized in Appendix A. The plane stress model described in this appendix is employed in the numerical analyses presented in Subsection 5.1.

In a two-dimensional setting, it is convenient to introduce a CARTESIAN coordinate system at $\boldsymbol{X}_0 \in \partial_{\mathrm{s}}\Omega$ via

$$\boldsymbol{N} \cdot \boldsymbol{m} = 0, \quad \text{and} \quad ||\boldsymbol{m}||_2 = 1. \tag{105}$$

According to Equation (105), $\boldsymbol{m}$ is orthogonal to the normal vector of the singular hyperplane $\partial_{\mathrm{s}}\Omega$. Hence, the shear component t_m of the traction vector $\boldsymbol{t} = \boldsymbol{\sigma} \cdot \boldsymbol{N}$ acting at $\partial_{\mathrm{s}}\Omega$ is written as

$$t_m = \boldsymbol{t} \cdot \boldsymbol{m}. \tag{106}$$

Assuming material failure to be governed only by the shear component of the traction vector, the yield function

$$\phi = |\boldsymbol{m} \cdot \boldsymbol{t}| - q(\alpha([\![\boldsymbol{u}]\!])) \tag{107}$$

represents a suitable choice (see also [13, 33] and compare to Appendix A). With Equation 107, and following Section 4, the weak form of traction continuity corresponding to inelastic loading leads to

$$\phi = |\boldsymbol{m} \cdot \overline{\boldsymbol{t}}| - q(\alpha([\![\boldsymbol{u}]\!])), \tag{108}$$

with $\overline{(\bullet)} := 1/V \int_\Omega (\bullet)\mathrm{d}V$. From Equation (108) and the assumption $\boldsymbol{\nabla}[\![\boldsymbol{u}]\!] = \boldsymbol{0}$, together with the principle of maximum dissipation, the evolution equation associated with the displacement discontinuity is obtained as

$$[\![\dot{\boldsymbol{u}}]\!] = \lambda\ \boldsymbol{m}\ \mathrm{sign}[\boldsymbol{m} \cdot \overline{\boldsymbol{t}}]. \tag{109}$$

Additionally, the rate of the internal variable α is computed as

$$\dot{\alpha} = \lambda. \tag{110}$$

Inserting Equations (109) and (110), into Equation (108) and applying a backward EULER integration, the discrete counterpart of Equation (108) is written as

$$\begin{aligned} \phi_{n+1} = & \Big| [\boldsymbol{m} \otimes \boldsymbol{N}] : [\overline{\boldsymbol{\sigma}^{\mathrm{tr}}_{n+1}} - \mathrm{sign}[\boldsymbol{m} \cdot \overline{\boldsymbol{t}}] \, \mathbb{C} : (\boldsymbol{m} \otimes \overline{\boldsymbol{\nabla}\varphi}) \, \Delta\lambda_{n+1}] \Big| \\ & - q(\alpha_n + \Delta\lambda_{n+1}) = 0. \end{aligned} \tag{111}$$

Equation (111) represents a nonlinear scalar-valued equation. As a consequence, it can be solved numerically, e.g. by means of NEWTON's method.
At a converged state, characterized by $\phi = 0$, the linearization of Equation (111) reads (compare to Equation (68))

$$\mathrm{d}\Delta\lambda_{n+1} = \frac{\mathrm{sign}[\boldsymbol{m} \cdot \overline{\boldsymbol{t}_{n+1}}] \; (\boldsymbol{m} \otimes \boldsymbol{N}) : \mathbb{C} : \mathrm{d}\overline{\boldsymbol{\nabla}^{\mathrm{sym}} \bar{\boldsymbol{u}}_{n+1}}}{(\boldsymbol{m} \otimes \boldsymbol{N}) : \mathbb{C} : (\boldsymbol{m} \otimes \overline{\boldsymbol{\nabla}\varphi}) - H_{n+1}}. \tag{112}$$

Hence, the linearization of the (local) stresses at $\boldsymbol{X}_i$, i.e.

$$\begin{aligned} \mathrm{d}\boldsymbol{\sigma}_{n+1}(\boldsymbol{X}_i) = \mathbb{C} : [& \mathrm{d}\boldsymbol{\nabla}^{\mathrm{sym}} \bar{\boldsymbol{u}}_{n+1}(\boldsymbol{X}_i) \\ & - \mathrm{sign}[\boldsymbol{m} \cdot \overline{\boldsymbol{t}_{n+1}}] \; (\boldsymbol{m} \otimes \boldsymbol{\nabla}\varphi(\boldsymbol{X}_i)) \; \mathrm{d}\Delta\lambda_{n+1}] \, , \end{aligned} \tag{113}$$

results in

$$\begin{aligned} \mathrm{d}\boldsymbol{\sigma}_{n+1}(\boldsymbol{X}_i) = & \quad \mathbb{C} : \mathrm{d}\boldsymbol{\nabla}^{\mathrm{sym}} \bar{\boldsymbol{u}}_{n+1}(\boldsymbol{X}_i) \\ & - \frac{\mathbb{C} : (\boldsymbol{m} \otimes \boldsymbol{\nabla}\varphi(\boldsymbol{X}_i)) \otimes (\boldsymbol{m} \otimes \boldsymbol{N}) : \mathbb{C}}{(\boldsymbol{m} \otimes \boldsymbol{N}) : \mathbb{C} : (\boldsymbol{m} \otimes \overline{\boldsymbol{\nabla}\varphi}) - H} : \mathrm{d}\overline{\boldsymbol{\nabla}^{\mathrm{sym}} \bar{\boldsymbol{u}}} \Big|_{n+1} . \end{aligned} \tag{114}$$

References

[1] T. Belytschko, J. Fish, and B.E. Engelmann. A finite element with embedded localization zones. *Computer Methods in Applied Mechanics and Engineering*, 70:59–89, 1988.

[2] R. De Borst. *Non-linear analysis of frictional materials*. PhD thesis, Technical University Delft, 1986.

[3] R. De Borst. Some recent issues in computational mechanics. *International Journal for Numerical Methods in Engineering*, 52:63–95, 2001.

[4] J. Simo, J. Oliver, and F. Armero. An analysis of strong discontinuities induced by strain softening in rate-independent inelastic solids. *Computational Mechanics*, 12:277–296, 1993.

[5] K. Garikipati and T.J.R. Hughes. A study of strain localization in a multiple scale framework - the one-dimensional problem. *Computer Methods in Applied Mechanics and Engineering*, 159(3-4):193–222, 1998.

[6] F. Armero. Large-scale modeling of localized dissipative mechanisms in a local continuum: applications to the numerical simulation of strain localization in rate-dependent inelastic solids. *Mechanics of Cohesive-Frictional Materials*, 4:101–131, 1999.

[7] N. Moës, J. Dolbow, and T. Belytschko. A finite element method for crack growth without remeshing. *International Journal for Numerical Methods in Engineering*, 46:131–150, 1999.

[8] M. Ortiz and E.A. Repetto. Nonconvex energy minimisation and dislocation in ductile single crystals. *J. Mech. Phys. Solids*, 47:397–462, 1999.

[9] C. Carstensen, K. Hackl, and A. Mielke. Non-convex potentials and microstructures in finite-strain plasticity. *Proc. R. Soc. Lond. A*, 458:299–317, 2002.

[10] C. Miehe and M. Lambrecht. Analysis of micro-structure development in shearbands by energy relaxation of incremental stress potentials: Large-strain theory for standard dissipative materials. *International Journal for Numerical Methods in Engineering*, 58:1–41, 2003.

[11] J. Simo and J. Oliver. A new approach to the analysis and simulation of strain softening in solids. In Z.P. Bažant, Z. Bittnar, M. Jirásek, and J. Mazars, editors, *Fracture and Damage in Quasibrittle Structures*, pages 25–39. E. &F.N. Spon, London, 1994.

[12] J. Oliver. Modelling strong discontinuities in solid mechanics via strain softening constitutive equations part 1: Fundamentals. part 2: Numerical simulations. *International Journal for Numerical Methods in Engineering*, 39:3575–3623, 1996.

[13] F. Armero and K. Garikipati. An analysis of strong discontinuities in multiplicative finite strain plasticity and their relation with the numerical simulation of strain localization in solids. *International Journal for Solids and Structures*, 33:2863–2885, 1996.

[14] G.N. Wells and L.J. Sluys. A new method for modelling cohesive cracks using finite elements. *International Journal for Numerical Methods in Engineering*, 50:2667–2682, 2001.

[15] R.I. Borja. A finite element model for strain localization analysis of strongly discontinuous fields based on standard galerkin approximation. *Computer Methods in Applied Mechanics and Engineering*, 190:1529–1549, 2000.

[16] M. Jirásek and T. Zimmermann. Embedded crack model: Part I: Basic formulation, Part II: Combination with smeared cracks. *International Journal for Numerical Methods in Engineering*, 50:1269–1305, 2001.

[17] J. Mosler and G. Meschke. 3D modeling of strong discontinuities in elastoplastic solids: Fixed and rotating localization formulations. *International Journal for Numerical Methods in Engineering*, 57:1533–1576, 2003.

[18] I. Babuška and J.M. Melenk. The partition of unity finite element method: Basic theory and applications. *Computer Methods in Applied Mechanics and Engineering*, 139:289–314, 1996.

[19] I. Babuška and J.M. Melenk. The partition of unity method. *International Journal for Numerical Methods in Engineering*, 40:727–758, 1997.

[20] T. Belytschko and T. Black. Elastic crack growth in finite elements with minimal remeshing. *International Journal for Numerical Methods in Engineering*, 45:601–620, 1999.

[21] N. Sukumar, N. Moës, B. Moran, and T. Belytschko. Extended finite element method for three-dimensional crack modelling. *International Journal for Numerical Methods in Engineering*, 48:1549–1570, 2000.

[22] J.C. Simo and S. Rifai. A class mixed assumed strain methods and the method of incompatible modes. *International Journal for Numerical Methods in Engineering*, 29:1595–1638, 1990.

[23] J.C. Simo and F. Armero. Geometrically non-linear enhanced strain mixed methods and the method of incompatible modes. *International Journal for Numerical Methods in Engineering*, 33:1413–1449, 1992.

[24] R. Larrson and K. Runesson. Element-embedded localization band based on regularized displacement discontinuity. *Journal of Engineering Mechanics (ASCE)*, 122:402–411, 1996.

[25] G.N. Wells and L.J. Sluys. Three-dimensional embedded discontinuity model for brittle fracture. *International Journal for Solids and Structures*, 38:897–913, 2001.

[26] J. Mosler and G. Meschke. 3D FE analysis of cracks by means of the strong discontinuity approach. In E. Oñate, G. Bugeda, and B. Suárez, editors, *European Congress on Computational Methods in Applied Sciences and Engineering*, 2000.

[27] J. Mosler and G. Meschke. FE-modeling of displacement discontinuities in inelastic continua. *Zeitschrift für Angewandte Mathematik und Mechanik*, 81(Suppl. 4):875–876, 2001.

[28] J. Simo and T.J.R. Hughes. *Computational inelasticity*. Springer, New York, 1998.

[29] J.C. Simo. Numerical analysis of classical plasticity. In P.G. Ciarlet and J.J. Lions, editors, *Handbook for numerical analysis*, volume IV. Elsevier, Amsterdam, 1998.

[30] J. Mosler and O.T. Bruhns. A 3D anisotropic elastoplastic-damage model using discontinuous displacement fields. *International Journal for Numerical Methods in Engineering*, 60:923–948, 2004.

[31] J. Mosler. *Finite Elemente mit sprungstetigen Abbildungen des Verschiebungsfeldes für numerische Analysen lokalisierter Versagenszustände in Tragwerken*. PhD thesis, Ruhr University Bochum, 2002.

[32] J. Mosler and G. Meschke. Embedded cracks vs. smeared crack models: A comparison of elementwise discontinuous crack path approaches with emphasis on mesh bias. *Computer Methods in Applied Mechanics and Engineering*, 193:3351–3375, 2003.

[33] K. Garikipati. *On strong discontinuities in inelastic solids and their numerical simulation*. PhD thesis, Stanford University, 1996.

[34] H. Matthies, G. Strang, and E. Christiansen. The saddle point of a differential program. In Glowinski, Robin, and Zienkiewicz, editors, *Energy methods in finite element analysis*, pages 309–318. J. Wiley and sons: London, 1979.

[35] R. Teman and G. Strang. Functions of bounded deformations. *Archive for Rational Mechanics ans Analysis*, 75:7–21, 1980.

[36] I. Stakgold. *Boundary value problems of mathematical physics*, volume I. Macmillien Series in Advanced Mathematics and theoretical physics, 1967.

[37] I. Stakgold. *Green's functions and boundary value problems*. Wiley, 1998.

[38] J. Oliver. Continuum modelling of strong discontinuities in solid mechanics. In D.R.J. Owen, E Oñate, and E. Hinton, editors, *Proc., 4th Int. Conf. Computational Plasticity*, volume 1, pages 455–479, 1995.

[39] R.I. Borja and A.R. Regueiro. Strain localization in frictional materials exhibiting displacement jumps. *Computer Methods in Applied Mechanics and Engineering*, 190:2555–2580, 2001.

[40] G.N. Wells and L.J. Sluys. Analysis of slip planes in three-dimensional solids. *Computer Methods in Applied Mechanics and Engineering*, 190:3591–3606, 2001.

[41] J. Mosler. Numerical analyses of discontinuous material bifurcation: Strong and weak discontinuities. *Computer Methods in Applied Mechanics and Engineering*, 194(9-11):979–1000, 2005.

[42] J. Oliver, A.E. Huespe, Samaniego E., and Chaves E.W.V. On Strategies for Tracking Strong Discontinuities in Computational Failure Mechanics. In H.A. Mang, F.G. Rammerstorfer, and J. Eberhardsteiner, editors, *Fifth World Congress on Computational Mechanics (WCCM V)*. Vienna University of Technology, Austria, 2002. ISBN 3-9501554-0-6, http://wccm.tuwien.ac.at.